A gridded dataset of leaf age-dependent LAI seasonality product (Lad-LAI) over tropical and subtropical evergreen broadleaved forests

Xueqin Yang[1,2,3], Xiuzhi Chen[1,*], Jiashun Ren[1,4], Wenping Yuan[1], Liyang Liu[5], Juxiu Liu[6], Dexiang Chen[7], Yihua Xiao[7], Qinghai Song[8], Yanjun Du[9], Shengbiao Wu[10], Lei Fan[11], Xiaoai Dai[4], Yunpeng Wang[3], and Yongxian Su[2]

[1]Guangdong Province Data Center of Terrestrial and Marine Ecosystems Carbon Cycle, Guangdong Province Key Laboratory for Climate Change and Natural Disaster Studies, School of Atmospheric Sciences, Sun Yat-sen University & Southern Marine Science and Engineering Guangdong Laboratory (Zhuhai), Zhuhai 519082, China

[2]Key Lab of Guangdong for Utilization of Remote Sensing and Geographical Information System, Guangdong Open Laboratory of Geospatial Information Technology and Application, Guangzhou Institute of Geography, Guangdong Academy of Sciences, Guangzhou 510070, China

[3]Guangzhou Institute of Geochemistry, Chinese Academy of Sciences, Guangzhou, 510640, China

[4]College of Earth Sciences, Chengdu University of Technology, Chengdu 610000, China;

[5]Laboratoire des Sciences du Climat et de l'Environnement, IPSL, CEA-CNRS-UVSQ, Université Paris-Saclay, 91191 Gif sur Yvette, France

[6]Dinghushan Forest Ecosystem Research Station, South China Botanical Garden, Chinese Academy of Sciences, Guangzhou 510650, China;

[7]Pearl River Delta Forest Ecosystem Research Station, Research Institute of Tropical Forestry, Chinese Academy of Forestry, Guangzhou 510650, China;

[8]CAS Key Laboratory of Tropical Forest Ecology, Xishuangbanna Tropical Botanical Garden, Chinese Academy of Sciences, Menglun, 666303, China;

[9]Key Laboratory of Genetics and Germplasm Innovation of Tropical Special Forest Trees and Ornamental Plants (Ministry of Education), College of Forestry, Hainan University, Haikou 570228, China

29   [10]School of Biological Sciences, The University of Hong Kong, Pokfulam, Hong Kong

30   [11]Chongqing Jinfo Mountain Karst Ecosystem National Observation and Research

31   Station, School of Geographical Sciences, Southwest University, Chongqing 400715,

32   China

33   *Correspondence: Xiuzhi Chen (chenxzh73@mail.sysu.edu.cn)*

Abstract

36   Quantification of large-scale leaf age-dependent leaf area index has been lacking

37   in tropical and subtropical evergreen broadleaved forests (TEFs) despite the recognized

38   importance of leaf age in influencing leaf photosynthetic capacity in this biome. Here,

39   we simplified the canopy leaves of TEFs into three age cohorts (i.e., young, mature and

40   old one with different photosynthesis capacities ($V_{c,max}$)) and proposed a novel

41   neighbor-based approach to develop the first gridded dataset of monthly leaf age-

42   dependent LAI product (**referred to as Lad-LAI**) at 0.25-degree spatial resolution over

43   the continental scale during 2001-2018 from satellite observations of sun-induced

44   chlorophyll fluorescence (SIF) that was reconstructed from MODIS and TROPOMI

45   (the TROPOspheric Monitoring Instrument). The new Lad-LAI products show good

46   performance in capturing the seasonality of three LAI cohorts, i.e., young (LAI_{young})

47   (the Pearson correlation coefficient, R=0.36), mature (LAI_{mature}) (R=0.77) and old

48   (LAI_{old}) (R=0.59) leaves at eight camera-based observation sites (four in south America,

49   three in subtropical Asia and one in Congo) and can also represent their interannual

50   dynamics, validated only at the Barrocolorado site with R being equal to 0.54, 0.64 and

51   0.49 for LAI_{young}, LAI_{mature} and LAI_{old}, respectively. Additionally, the abrupt drops in

52   LAI_{old} are mostly consistent with the seasonal litterfall peaks at 53 *in situ* measurements

53   across the whole tropical region (R=0.82). The LAI seasonality of young and mature

54   leaves also agrees well with the seasonal dynamics of Enhanced Vegetation Index (EVI)

55   (R=0.61), a proxy of photosynthetically effective leaves. Spatially, the gridded Lad-

56   LAI data capture a dry-season green-up of canopy leaves across the wet Amazonia areas

where mean annual precipitation exceeds 2,000 mm yr^{-1}, consistent with previous satellite-based analyses. The spatial patterns clustered from the three LAI cohorts also coincide with those clustered from climatic variables over the whole TEF region. Herein, we provide the average seasonality of three LAI cohorts as the main dataset, and their time-series as a supplementary dataset. These Lad-LAI products are available at https://doi.org/10.6084/m9.figshare.21700955.v4 (Yang et al., 2022).

1. Introduction

Tropical and subtropical evergreen broadleaved forests (TEFs) account for approximately 34% of global terrestrial primary productivity (GPP) (Beer et al., 2010) and 40-50% of the world's gross forest carbon sink (Pan et al., 2011; Saatchi et al., 2011). Despite a perennial canopy, TEFs shed and rejuvenate their leaves continuously throughout the year, leading to significant seasonality in canopy leaf demography (Wu et al., 2016; Chen et al., 2021). This phenological change in leaf demography is the primary cause of GPP seasonality in TEFs (Saleska et al., 2003; Sayer et al., 2011; Leff et al., 2012) and thus largely regulates their seasonal carbon sinks (Beer et al., 2010; Aragao et al., 2014; Saatchi et al., 2011).

A key plant trait linking canopy phenology with GPP seasonality was shown to be leaf age (Wu et al., 2017; Xu et al., 2017). At leaf scale, the newly-flushed young leaves and maturing leaves show higher maximum carboxylation rates ($V_{c,max}$) than the old leaves being replaced (De Weirdt et al., 2012; Chen et al., 2020). Such age-dependent variations in $V_{c,max}$ are associated with changes in leaf nutritional contents (nitrogen, phosphorus and potassium, etc.) and stomatal conductance over time (Menezes et al., 2021). Xu et al. (2017) and Menezes et al. (2021) monitored *in situ* leaf age and leaf demography combined with leaf-level $V_{c,max}$ in Amazonian TEFs and found that $V_{c,max}$ of newly-flushed leaves increases rapidly with leaf longevity, peaks at approximately 2-month old, and then declines gradually as leaf grows older (leaf age > 2 months). At canopy scale, it was hypothesized that leaf demography and seasonal differences in leaf

85   age compositions of tree canopies control the GPP seasonality in TEFs (Wu et al., 2016;

86   Albert et al., 2018). A similar mechanism was also observed from the ground-based

87   LiDAR signals which showed an increasing trend in upper canopy leaf area index (LAI)

88   during the dry season, whereas a decrease in lower canopy LAI (more old leaves)

89   (Smith et al., 2019). Wu et al. (2016) classified canopy leaves of Amazonian TEFs into

90   three leaf age cohorts (young: 1-2 months, mature: 3-5 months and old: $\geq$ 6 months).

91   LAI of young and mature leaves increased during the dry seasons and consequently

92   promoted dry-season canopy photosynthesis. Based on above age-dependent $V_{c,max}$ at

93   leaf scale (Xu et al., 2017) and LAI seasonality of different leaf age cohorts at canopy

94   scale (Wu et al., 2016), Chen et al. (2020; 2021) developed a climate-triggered leaf

95   litterfall and flushing model and successfully represented the seasonality of canopy leaf

96   demography and GPP at four Amazonian TEF sites. Overall, leaf age-dependent LAI

97   seasonality is one of the vital biotic factors in influencing the GPP seasonality in TEFs

98   (Wu et al., 2016; Chen et al., 2020).

99   Although the leaf age-dependent LAI seasonality can be well documented at site

100   level using phenology cameras (Wu et al., 2016), it is still rarely studied and remains

101   unclear at the continental scale. The key causation is that leaf flushing and litterfall of

102   TEFs in different climatic regions experience different seasonal constraints of water

103   and light availability during recurrent dry and wet seasons (Brando et al., 2010; Chen

104   et al., 2020; Davidson et al., 2012; Xiao et al., 2005). Thus, the seasonal patterns of LAI

105   in different leaf age cohorts become very complex at the continental scale (Chen et al.,

106   2020; Xu et al., 2015). Satellite-based remote sensing (Saatchi et al., 2011, Guan et al.,

107   2015) and land surface model (LSM) technologies (De Weirdt et al., 2012; Chen et al.,

108   2020; 2021) are two commonly used approaches for detecting the spatial heterogeneity

109   of plant phenology at a large scale. However, for satellite-based studies, most optical

110   signals are saturated in TEFs due to the dense covered canopies and thus fail to capture

111   the seasonality of total LAI in TEFs, much less decomposing the LAI into different leaf

112   age cohorts. These limitations prevent satellite-based studies from accurately

representing the age-dependent LAI seasonality. Moreover, most ESM models also show poor performances in simulating the LAI seasonality in different leaf age cohorts (De Weirdt et al., 2012; Chen et al., 2020). This is because the underlying mechanisms linking seasonal water and light availability with leaf flushing and litterfall seasonality are currently highly debated and remain elusive at the regional scale (Leff et al., 2012; Saleska et al., 2003; Sayer et al., 2011). This vague notion imposes a challenge for accurately modeling continental-scale GPP seasonality in most LSMs (Restrepo-Coupe et al., 2017; Chen et al., 2021).

To fill the research gap, this study aimed to produce a global gridded dataset of leaf age-dependent LAI seasonality product (Lad-LAI) over the whole TEF biomes from 2001 to 2018. For this purpose, we first simplified that canopy GPP was composed of three parts that were produced from young, mature and old leaves, respectively. GPP was then expressed as a function of the sum of the product of each LAI cohort (i.e., young, mature and old leaves, denoted as LAI_{young}, LAI_{mature}, and LAI_{old}, respectively) and corresponding net CO_2 assimilation rate (An, denoted as An_{young}, An_{mature}, and An_{old} for young, mature and old leaves, respectively) (**Equation 1**). Then, we proposed a novel neighbor-based approach to derive the values of three LAI cohorts. It was hypothesized that forests in adjacent four cells in the gridded map exhibited consistent seasonality in both GPP, and LAI cohorts (LAI_{young}, LAI_{mature}, and LAI_{old}). Based on this assumption, we applied **Equation 1** to each pixel and combined the four equations of 2*2 neighboring pixels to derive the three LAI cohorts using a linear least-squares with constrained method. An was calculated using the Farquhar-von Caemmerer-Berry (FvCB) leaf photochemistry model (Farquhar et al., 1980); and GPP was linearly derived from an arguably better proxy—TROPOMI (the TROPOspheric Monitoring Instrument) Solar-Induced Fluorescence (SIF) based on a simple SIF-GPP relationship established by Chen et al. (2022) (see **Methods** for details). This gridded dataset of three LAI cohorts provides new insights into tropical and subtropical phenology with more details of sub-canopy level of leaf seasonality in different leaf age cohorts and

141 will be helpful for developing an accurate tropical phenology model in ESMs.

142

2. Study area and material

2.1 Tropical and subtropical evergreen broadleaved forest biomes

145 In this study, we focused on the whole tropical and subtropical evergreen broadleaf

146 forests (TEFs). The pixels labeled TEFs according to the International Geosphere-

147 Biosphere Program (IGBP) classification were extracted as the study area based on the

148 0.05° spatial resolution MODIS land cover map (**Fig. 1**) (MCD12C1, Sulla-Menashe et

149 al., 2018). The study area contains three regions: South America (30°S–18°N; 40°W–

150 90°W), the world's largest and most biodiverse tropical rain forest, Congo (10°S–10°N;

151 10°W−30°E), the western part of the Africa TEF region, and Tropical Asia (20°S–30°N;

152 70°E−150°E), covering the Indo-China Peninsula, the majority of the Malay

153 Archipelago and northern Australia.
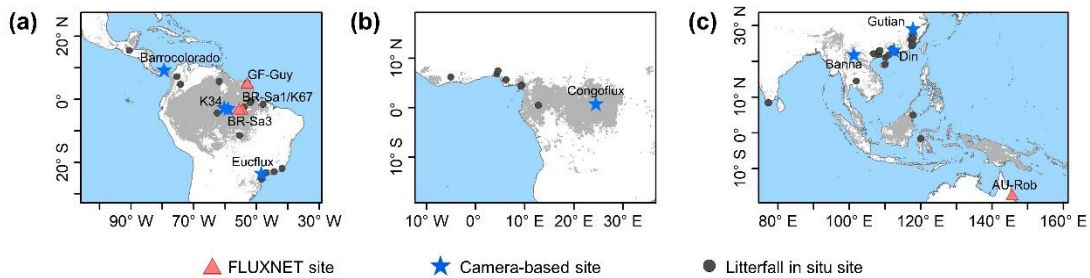
154

155 **Figure 1.** Study areas over tropical and subtropical evergreen broadleaves forests (TEF).

156 Red triangles: observed GPP seasonality at four eddy covariance (EC) tower sites. Blue

157 pentangles: observed LAI cohorts at eight camera-based observation sites. Black circles:

158 observed litterfall seasonality at 53 observation sites.

159

2.2 Input datasets for calculating GPP and An parameters

161 The TROPOspheric Monitoring Instrument (TROPOMI) Solar-Induced

162 Fluorescence (SIF) data were used to derive the continent-scale GPP (denoted as

163 RTSIF-derived GPP) according to the SIF-GPP relationship established by Chen et al.

164 (2022) which used 15.343 as a transformation coefficient to covert SIF to GPP. The air

temperature data from ERA5-Land (Zhao, Gao et al., 2020), vapor pressure deficits (VPD) data from ERA-Interim (Yuan et al., 2019) and downward shortwave solar radiation (SW) from Breathing Earth System Simulator (BESS) (Ryu et al., 2018) were used to calculate K_C, K_O, Γ^*, R_{dark} and $V_{c,max}$ and thus to calculate An according to equations in **Table S4**. The calculation processes were illustrated in **Fig. 2**. All datasets were aggregated at the same spatial (0.125°) and temporal resolutions (month) (**Table S3**).

2.3 Datasets for validating leaf age-dependent LAI seasonality

Ground-based seasonal LAI cohorts and litterfall data. Top-of-canopy imageries observed by ground-based phenology cameras were used to decompose canopy LAI into LAI_{young}, LAI_{mature} and LAI_{old}. In total, imageries from eight observation sites across the whole TEF region were used to validate the simulating results (blue pentangles in **Fig. 1**, **Table S1**). Additionally, the seasonal litterfall data from 53 *in situ* sites (black circles in **Fig. 1**, **Table S6**) spanning the TEFs were collected from globally published articles to compare with the phase of simulated LAI_{old} seasonality (see **Methods** for details). The multiyear monthly litterfall data were averaged to the monthly mean to compare with the seasonality of simulated LAI_{old}. Four eddy covariance flux tower sites (red triangles in **Fig. 1**, **Table S2**) provided *in situ* seasonal GPP data to evaluate the seasonality of RTSIF-derived GPP.

Satellite-based seasonal EVI data. To evaluate the LAI seasonality of photosynthesis-effective leaves, i.e., young and mature leaves, this study used satellite-based MODIS Enhanced Vegetation Index (EVI) (Huete et al., 2002; Lopes et al., 2016; Wu et al., 2018) as a remotely sensed proxies alternatives of effective leaf area changes and new leaf flush, i.e., $LAI_{young+mature}$ (Wu et al., 2016; Xu et al., 2015). To prove the robustness of the products over a large spatial coverage, the seasonal LAI cohorts of young and mature leaves were evaluated against the enhanced vegetation index (EVI) product, which was considered as a proxy for leaf area changes of photosynthetically

193 effective leaves (Xu et al., 2015; Wu et al., 2016; de Moura et al., 2017).

194

3. Methods

3.1 Decomposing LAI cohorts (young, mature and old) from SIF-derived GPP

197 **Figure 2** illustrates the overall framework used to generate leaf age-dependent LAI

198 seasonality product (Lad-LAI). The majority of the tropical and subtropical EBFs retain

199 leaves year-round and their total LAI shows marginally small spatial and seasonal

200 changes (Wu et al., 2016) (**Figs. S3, S4**). Therefore, previous modelling studies have

201 assumed a constant value for the total LAI in tropical and subtropical EBFs (Cramer et

202 al., 2001; Arora and Boer, 2005; De Weirdt et al., 2012). Based on this, we collected

203 observed seasonal LAI dynamics in tropical and subtropical EBFs from previously

204 published literatures which showed a constant value of LAI around 6.0 (**Figs. S3**, **S4**,

205 **Table S5**). Thus, in this study, we simplified to assume that the seasonal LAI was

206 approximately equal to 6.0 in tropical and subtropical EBFs. We grouped the canopy

207 leaves of tropical and subtropical EBFs into three leaf age cohorts, i.e., young, mature

208 and old leaves, respectively. Then, the total GPP was defined as the sum of those

209 produced by the young, mature and old leaves, respectively. According to the Farquhar-

210 von Caemmerer-Berry (FvCB) leaf photochemistry model (Farquhar et al., 1980), GPP

211 can be expressed as function of the sum of the products of each LAI cohort (LAI_{young},

212 LAI_{mature}, and LAI_{old}) and corresponding net CO_2 assimilation rate (An_{young}, An_{mature},

213 and An_{old}) (**Equation 1**).

214 $$GPP = LAI_{young} \times An_{young} + LAI_{mature} \times An_{mature} + LAI_{old} \times An_{old} \quad (1)$$

215 where LAI_{young}, LAI_{mature} and LAI_{old} are the leaf area index of young, mature and old

216 leaves, respectively; An_{young}, An_{mature} and An_{old} are the net rate of CO_2 assimilation

217 dependent on three leaf age classes; GPP is canopy total gross primary production. The

218 sum of LAI_{young}, LAI_{mature} and LAI_{old} was set as a constant in this study, equaling to 6.0.

219 The gridded GPP data over the whole EBFs were derived from SIF (denoted as

220 RTSIF-derived GPP) using a linear SIF-GPP regression model (see sect. 3.2) which was

221   established based on *in situ* GPP from 76 eddy covariance (EC) sites (Chen et al., 2022).

222   The An_{young}, An_{mature} and An_{old} were calculated according to the FvCB biochemical

223   model (Farquhar et al., 1980; Bernacchi et al., 2003) (see section 3.3). As there were

224   three unknown variables (i.e., LAI_{young}, LAI_{mature} and LAI_{old}) to be solved in **Equation**

225   **1**, we hypothesized that the adjacent four pixels exhibited homogenous EBFs and

226   consistent leaf demography and canopy photosynthesis. Then, we used the GPP and An

227   data from adjacent four pixels to estimate their LAI_{young}, LAI_{mature} and LAI_{old} based on

228   **Equation 1** using a linear least-squares with constrained method. The inputs gridded

229   datasets (i.e., RTSIF-derived GPP and An derived from T_{air}, VPD and SW) (**Table S3,**

230   **Fig. 2**) were sampled at 0.125-degree spatial resolution; while the output maps of

231   LAI_{young}, LAI_{mature}, and LAI_{old} were at 0.25-degree spatial resolution. Therefore, the

232   output maps of LAI_{young}, LAI_{mature}, and LAI_{old} were at a 0.25-degree spatial resolution.

233   Additionally, to test the robustness of the neighbor-based decomposition approach, we

234   increased the number of adjacent pixels from 4 (2*2) to 16 (4*4) to produce another

235   version of Lad-LAI products with a spatial resolution of 0.5-degree. All our analyses

236   were conducted using Python (version 3.7, http://www.python.org) and Matlab (version

237   R2019b) software.

238
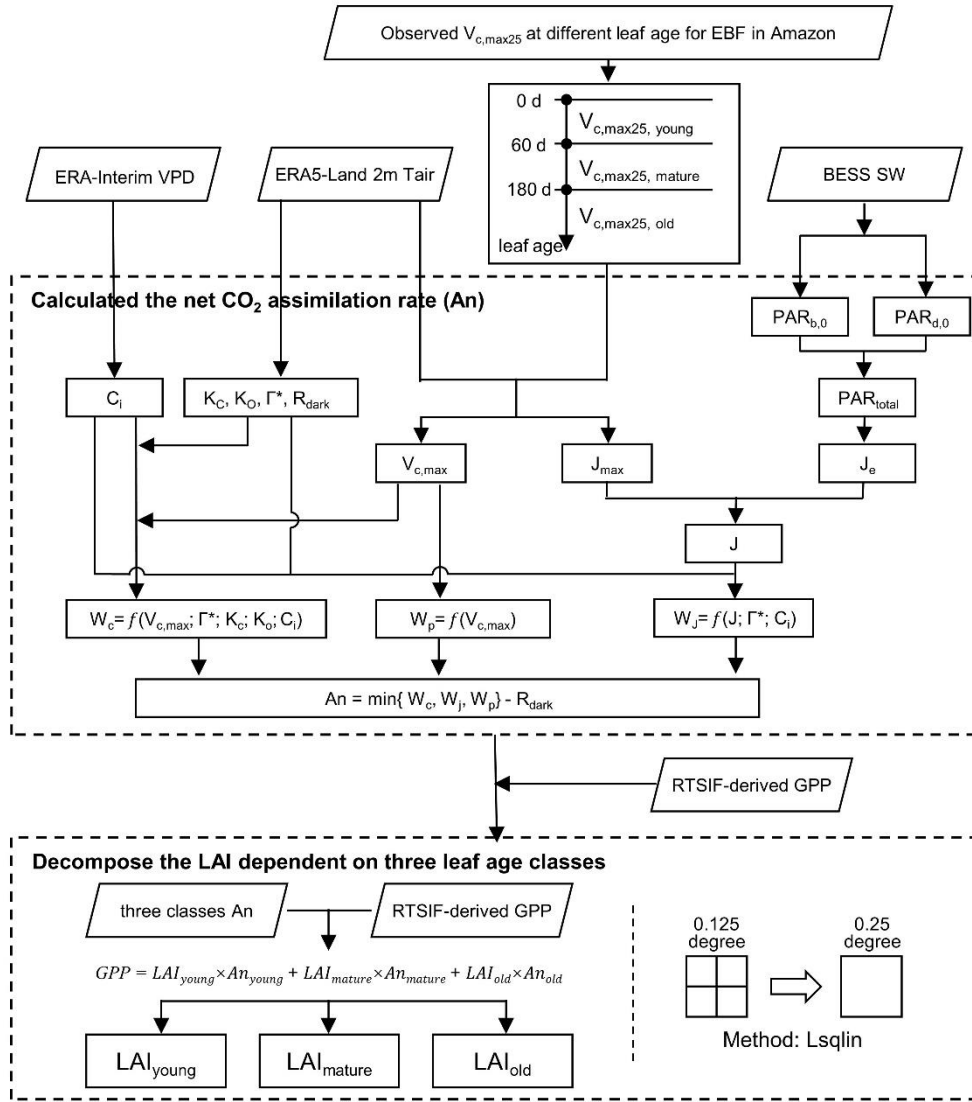
Figure 2. The workflow for mapping Lad-LAI using the Lsqlin method. Lsqlin is the

abbreviation of Linear least-squares solver with bounds or linear constraints. All the

abbreviations were described in supplementary **Tables S4**.

242

3.2 Calculating the GPP (RTSIF-derived GPP) from TROPOMI SIF

Satellite-retrieved solar-induced chlorophyll fluorescence (SIF) is a widely used

proxy for canopy photosynthesis (Yang et al., 2015; Dechant et al., 2020). Here, we

used a long-term reconstructed TROPOMI SIF dataset (RTSIF) (Chen et al., 2022) to

estimate GPP seasonality. Previous analyses showed that RTSIF was strongly linearly

correlated to eddy covariance (EC) GPP and used 15.343 as a transformation coefficient

to convert RTSIF to GPP (Fig. 8a in Chen et al., 2022). In this study, we followed

previously published literatures to set a constant value of LAI around 6.0 for the whole

tropical and subtropical EBFs (**Figs. S3**, **S4**, **Table S5**). We collected seasonal GPP data

observed at four EC sites from the FLUXNET 2015 Tier 1 dataset (**Table S2**; Pastorello

et al., 2020) and validated the Chen's simple SIF-GPP relationship (**Fig. S1**). Results

confirmed the robustness of Chen's simple SIF-GPP relationship in estimating the GPP

seasonality in tropical and subtropical EBFs (R>0.49). Despite potential overestimation

(**Fig. S1 b**) or underestimation (**Fig. S1 h**) of the magnitudes, RTSIF-derived GPP

mostly captured the seasonality of the EC GPP at all four sites (d_{phase} < 0.26).

3.3 Calculating the net rate of CO_2 assimilation (An)

We calculated the net CO_2 assimilation (An) using the FvCB biochemical model

(Farquhar et al., 1980). In this model, the parameter An was calculated as the minimum

of Rubisco (W_c), RuBP regeneration (W_j) and TPU (W_p) to minus dark respiration (R_{dark})

(Bernacchi et al., 2013). The formulas for calculating An, W_c, W_j, W_p, R_{dark} and

corresponding intermediate variables were listed in **Tables S4**.

Calculation of W_c. W_c is expressed as a function of internal CO_2 concentration (c_i),

Michaelis-Menton constant for carboxylase (K_c), Michaelis-Menton constant for

oxygenase (K_o), CO_2 compensation point (Γ^*) and maximum carboxylation rate ($V_{c,max}$)

(**Table S4-part1**) (Lin et al., 2015; Bernacchi et al., 2013; Ryu et al., 2011; Medlyn et

al., 2011; June et al., 2004; Farquhar et al., 1980). The K_c, K_o, Γ^* and $V_{c,max}$ are

temperature-dependent variables. Thus, we used **Equation 2** to calculate their values at

T_k by converting from those at 25°C. Then, we used the Medlyn's stomatal conductance

model (Medlyn et al., 2011) to estimate internal CO_2 concentration (c_i) (**Equation 3**),

which is expressed as a function of vapor pressure deficit (VPD) rather than relative

humidity (Lin et al., 2015). The method for calculating the $V_{c,max}$ of each LAI cohort

was introduced in section 3.4. The formulas for calculating corresponding intermediate

parameters were presented in **Table S4**.

277 $$Para = Para_{25} \times exp\left(\frac{(T_k - 298.15) \times \Delta H_{para}}{R \times T_k \times 298.15}\right) \qquad (2)$$

278 where *Para* denotes a correction factor arising from the temperature dependence of

279 $V_{c,max}$; $Para_{25}$ are values of the temperature-dependent parameters (K_c, K_o, Γ^* and $V_{c,max}$)

280 at the temperature 25°C; T_k denotes temperature in Kelvin; ΔH_{para} is the activation

281 energy for temperature dependence; R is the universal gas constant.

282 $$c_i = c_a \times \left(1 - \frac{1}{1.6 \times \left(1 + \frac{g_1}{\sqrt{VPD}}\right)}\right) \qquad (3)$$

283 where c_a is atmospheric CO_2 concentration, 380 ppm; VPD was calculated from air

284 temperature and dew point temperature of the global ERA-Interim reanalysis dataset

285 (Dee et al., 2011) using the method of Yuan et al. (2019). The calculation formula of

286 VPD was described in supplementary files. In this study, we used the value of 3.77 for

287 the stomatal slope (g_1) in the stomatal conductance model according to Lin et al. (2015).

288   ***Calculation of W_p.*** W_p was calculated as the function of $V_{c,max}$, which was given

289 different values for different LAI cohorts based on multiple *in situ* observations (section

290 3.4).

291   ***Calculation of W_j.*** W_j was calculated from $V_{c,max}$, c_i and the rate of electrons

292 through the thylakoid membrane (J) (Bernacchi et al., 2013). The parameter J was

293 calculated from the maximum electron transport rate (J_{max}) and the rate of whole

294 electron transport provided by light (J_e) (Bernacchi et al., 2013). J_{max} was expressed as

295 a temperature dependence function of maximum electron transport rate ($J_{max,25}$) at 25°C

296 and temperature (T_{air}) and J_e was expressed as a function of total PAR absorbed by

297 canopy (PAR_{total}) that was the sum of active radiation in beam ($PAR_{b,0}$) and diffuse

298 ($PAR_{d,0}$) light firstly (Weiss et al., 1985), which were calculated from downward short-

299 wave radiation (SW) (Ryu et al., 2018). The formula for PAR_{total} was given in **Equation**

300 **4** and formulas for other intermediate parameters (i.e., $PAR_{b,0}$, $PAR_{d,0}$, ρ_{cb}, ρ_{cd}, k'_b, k'_d,

301 and CI) were listed in **Table S4**.

302 $PAR_{total} = (1 - \rho_{cb}) \times PAR_{b,0} \times \left(1 - exp(-k'_b \times CI \times LAI_{total})\right) + (1 - \rho_{cd}) \times$

303 $PAR_{d,0} \times \left(1 - exp(-k'_d \times CI \times LAI_{total})\right) \qquad (4)$

304 where PAR_{total} is total PAR absorbed by canopy; $PAR_{b,0}$ is the active radiation; $PAR_{d,0}$

305 is diffuse radiation; LAI_{total} is a total LAI. Here, we used a constant value of 6.0

306 according to De Weirdt et al. (2012).

307

3.4 Classifying three LAI cohorts with different $V_{c,max}$

309 In this study, we collected *in situ* samples of $V_{c,max25}$ data against different leaf age

310 across tropical and subtropical EBFs from previous publications. Mature leaves (leaf

311 age: 70-160 days) show the highest $V_{c,max25}$ than those of newly flushed leaves (leaf age:

312 <60 days) and old leaves(leaf age: >200 days) as Menezes et al. (2021). Therefore, in

313 this study, we classified the canopy leaves into three cohorts: young (leaf age: <2

314 months), mature (leaf age: 3-5 months) and old cohorts (leaf age: >6 months) as Wu et

315 al. (2016). The $V_{c,max25}$ for young, mature and old cohorts were set as 60, 40 and 20

316 $\mu mol\ m^{-2}\ s^{-1}$, respectively, according to previous ground-based observations by Chen et

317 al. (2020).

318

3.5 Decomposing camera-based LAI into three leaf age cohorts

320 We classified the canopy leaves into young, mature and old age cohorts based on

321 the green-color band from the top-of-canopy imageries observed by RGB camera. It is

322 because the brightness of different leaf age leaves differs greatly in the values of the

323 green-color band. Raster density slicing is a useful classification method for detecting

324 the attributes of various ground objects (Kartikeyan et al., 1998). Therefore, we set three

325 brightness thresholds to divide young (blue), mature (green), old (yellow) leaves and

326 background (gray) for the same canopy extent in each month (**Fig. S2**). This analysis

327 was conducted in ENVI5.3 software.

328

3.6 Evaluating the $LAI_{young+mature}$ seasonality and its spatial patterns using

satellite-based EVI products

331 To compare the seasonality of $LAI_{young+mature}$ with those of EVI, we calculate mean

squared deviation (MSD) and their three components—d_{bias}, which denotes the differences about absolute value, d_{var}, which denotes the differences of seasonal fluctuations, and d_{phase}, which denotes the differences of peak phase to evaluate this consistency, comprehensively (see section 3.8). Additionally, we compared the spatial patterns of the wet- minus dry-season differences (Δ) between observed and simulated variables, following the work of Guan et al. (2015). To determine the wet and dry seasons in each grid cell, we defined a month as dry one when its monthly average precipitation was smaller than the potential evapotranspiration (PET) computed using the method of Maes et al. (2019); other months were classified as wet ones. The wet-minus dry-season $LAI_{young+mature}$ (denoted as $\Delta LAI_{young+mature}$) was calculated for each grid cell as the wet-season average $LAI_{young+mature}$ value minus the dry-season average value of $LAI_{young+mature}$.

3.7 Evaluating the LAI_{old} seasonality using ground-based litterfall data

Litterfall is closely related to the seasonal dynamics of old leaves, i.e., LAI_{old} (Chen et al., 2020; Yang et al., 2021). Previous analyses indicated that, in general, a sharping decrease in LAI_{old} corresponded to a peak in litterfall (Pastorello et al., 2020; Midoko Iponga et al., 2019; Ndakara, 2011; Barlow et al., 2007; Dantas and Phillipson, 1989). Based on this causal relationship between litterfall and LAI_{old}, we compared the time of seasonal litterfall peak with the time of abrupt drops in LAI_{old}, to indirectly evaluate the simulated LAI_{old} seasonality. To accurately detect the onset date of old leaves shedding and the day of litterfall peak, we used a least-square regression analysis method developed by Piao et al. (2006) to smoothen LAI_{old} and litterfall seasonal curves. The sixth-degree polynomial function (n=6) was applicable to the regression (**Equation 5**).

$$LAI_{old} = a_0 + a_1 x + a_2 x^2 + a_3 x^3 + a_4 x^4 + a_5 x^5 + a_6 x^6 \qquad (5)$$

where x is the day of a year.

The slope of seasonal LAI ($LAI_{old, ratio}$) was calculated in **Equation 6**. The date of

360   abrupt drops in LAI_{old} was defined as the time with most negative values of $LAI_{old, ratio}$.

361    $$LAI_{old,ratio(t)} = \left(LAI_{old(t+1)} - LAI_{old(t)}\right)/\left(LAI_{old(t)}\right) \qquad (6)$$

362   where $LAI_{old, ratio}$ is the slope of seasonal LAI_{old} curve. $LAI_{old(t+1)}$ and $LAI_{old(t)}$ are the

363   corresponding monthly LAI at time t+1 and t, respectively.

364

365   **3.8 Evaluation Metrics**

366   Two metrics were chosen to evaluate the seasonality of Lad-LAI against the that of

367   other proxies: the Kobayashi decomposition of the Mean Square Difference between

368   model and observation (Kobayashi and Salam, 2000) and the Pearson correlation

369   coefficient (Pearson, 1896) for gridded fields.

370   *Mean squared deviation (MSD).* The mean squared deviation (MSD) was given

371   by Kobayashi and Salam (2000):

372    $$MSD = \frac{1}{n}\sum_{i=1}^{n}(x_i - y_i)^2 \qquad (7)$$

373    $$SB = (\bar{x} - \bar{y})^2 \qquad (8)$$

374    $$SD_s = \sqrt{\frac{1}{n}\sum_{i=1}^{n}(x_i - \bar{x})^2} \qquad (9)$$

375    $$SD_m = \sqrt{\frac{1}{n}\sum_{i=1}^{n}(y_i - \bar{y})^2} \qquad (10)$$

376    $$SDSD = (SD_s - SD_m)^2 \qquad (11)$$

377    $$LCS = 2SD_sSD_m(1 - r) \qquad (12)$$

378   where mean squared deviation is the square of RMSD; i.e., MSD = RMSD^2; and x_i is

379   the simulated data at time t, and y_i is the observed one at time t (month). The lower the

380   value of MSD, the closer the simulation is to the measurement. MSD can be

381   decomposed into the sum of three components: the squared bias (d_{bias}), $d_{bias}=SB$; the

382   squared difference between standard deviations (variance-related difference, d_{var}),

383    $d_{var}=SDSD$; and the lack of correlation weighted by the standard deviations (phase-

384   related difference, d_{phase}), $d_{phase}=LCS$; r indicates the correlation coefficient between x

385   and y.

386   *Pearson correlation coefficient (R).* The Pearson correlation coefficient is a

387   measure of linear correlation between two variables (Merkl and Waack, 2009). The

388   correlation coefficient between X and Y was as:

389     $\rho_{X,Y} = \frac{cov(X,Y)}{\sigma_X \sigma_Y} = \frac{E((X-\mu_X)(Y-\mu_Y))}{\sigma_X \sigma_Y}$ (13)

390

3.9 The quality control (QC) for the Lad-LAI product

392   We provided information of data quality control (QC) along with the Lad-LAI

393   product (**Fig. S5**). In the QC system (**Table S7**), data quality was divided into four

394   levels: level 1 represents the highest quality; level 2 and level 3 represent good and

395   acceptable quality, respectively; and level 4 warns to be used cautiously. This QC

396   product was generated according to residual sum of squares (RSS) (Melgosa et al., 2008)

397   and the root mean square error (RMSE) (Chen et al., 2020), obtained from the

398   constrained least-squares method that was used to estimate derive monthly Lad-LAI

399   data.

400

4. Results

4.1 Comparison of LAI cohort seasonality with site observations

403   The simulated leaf age-dependent LAI seasonality product was validated against

404   the camera-based measurements of LAI_{young}, LAI_{mature}, and LAI_{old} at four sites in south

405   America, one site in Congo and three sites in China. Overall, the LAI seasonality of

406   mature and old classes from the new Lad-LAI products agrees well at these sites with

407   very fine-scale collections of monthly LAI of mature (R=0.77, MSD=0.69) and old

408   leaves (R=0.59, MSD=0.62). However, the seasonality of simulated LAI from young

409   leaves performs a little poor (R=0.36, MSD=0.45). It is also interesting to note that the

410   canopy leaf phenology of TEFs at these sites differ greatly. In south America, at K67,

411   K34 and Eucflux sites, both *in situ* and simulated LAI_{young} and LAI_{mature} decrease at

412   early dry season around February and convert to increase at early wet season around

413   June (**Fig. 3 a, b, d, e, j, k**). At the Barrocolorado site, LAI_{young} increases from the late

414   dry to early wet season around Mar in response to the increasing incoming shortwave

415 radiation and in contrast, LAI_{mature} starts to increase at wet season around June (**Fig. 3**

416 **g, h**). However, in subtropical Asia, LAI_{young} and LAI_{mature} increase during the wet

417 season and peak with largest rainfall at June or July at Din, Gutian and Banna sites (**Fig.**

418 **5 a, b, d, e, g, h**). In Congo, we only found one site (Congoflux) with six months

419 observation period (from May to October). The seasonality of LAI_{young} and LAI_{mature}

420 are similar as those in tropical Asia while having smaller variations in magnitude due

421 to the moderate seasonality of sunlight in the Equator region (**Fig. 4 a, b**). Overall, there

422 is a reverse pattern for LAI_{old} seasonality compared to LAI_{mature} for all the eight sites.

423

424
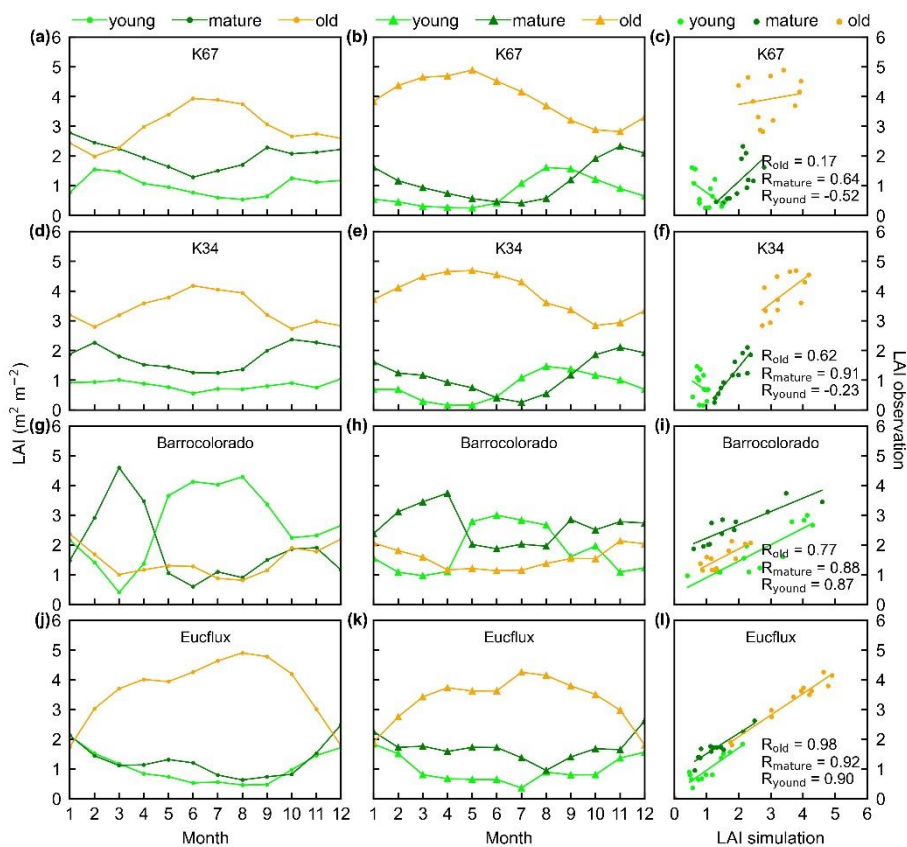
Figure 3. Seasonality of simulated LAI_{young}, LAI_{mature}, and LAI_{old} in comparison with observed data at 4 sites in south America. (Panels a, d, g and j) simulated LAIs; (panels b, e, h and k) observed LAIs; (panels c, f, i and l) scatterplots between simulated and observed LAIs. Limegreen dots are LAI_{young}; green dots are LAI_{mature}; orange dots are LAI_{old}.

430
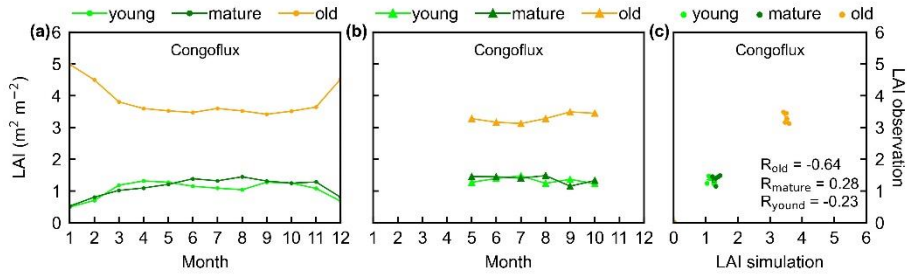
Figure 4. Seasonality of simulated LAI$_{young}$, LAI$_{mature}$, and LAI$_{old}$ in comparison with observed data at one site in Congo. (a) Simulated LAIs; (b) observed LAIs; and (c) scatterplots between simulated and observed LAIs. Limegreen dots are LAI$_{young}$; green dots are LAI$_{mature}$; orange dots are LAI$_{old}$.

435
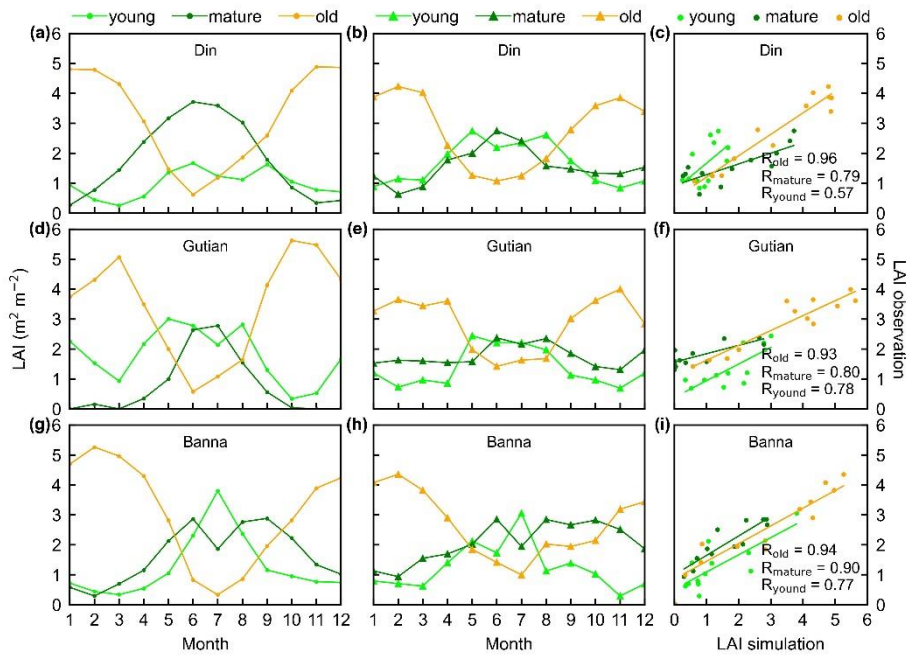
Figure 5. Seasonality of simulated LAI$_{young}$, LAI$_{mature}$, and LAI$_{old}$ in comparison with observed data at 3 sites in tropical Asia. (Panels a, d and g) simulated LAIs; (panels b, e and h) observed LAIs; (panels c, f and i) scatterplots between simulated and observed LAIs. Limegreen dots are LAI$_{young}$; green dots are LAI$_{mature}$; orange dots are LAI$_{old}$.

440

Additionally, only one ground site (Barrocolorado site in Panama) had observed time-series camera-based phenological imageries, which were then used to evaluate the capacity of Lad-LAI in representing the interannual dynamics of three LAI cohorts, with R values being equal to 0.54, 0.64, 0.49 for LAI$_{young}$, LAI$_{mature}$, LAI$_{old}$, respectively

445 (**Fig. 6**). However, more *in situ* long-term observations are in need to test the robustness

446 of the time-series variations. The temporal variations of LAI$_{young}$, LAI$_{mature}$, LAI$_{old}$

447 across 8 sub-regions classified by the *K*-means clustering analysis were shown in **Fig.**

448 **S6**. Results showed that, for example, the LAI$_{mature}$ increased significantly due to 2015

449 drought in Amazon basin (e.g., sub-region S2, **Fig. S6**) and southeast Asia (e.g., sub-

450 region S7, **Fig. S6**), indicating good capability of detecting the dynamics of LAI$_{young}$,

451 LAI$_{mature}$, LAI$_{old}$ in response to climate disturbances.
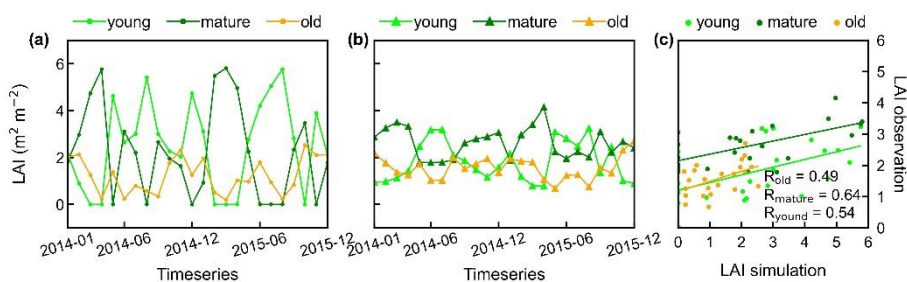
452

453 **Figure 6.** Timeseries of simulated LAI$_{young}$, LAI$_{mature}$, and LAI$_{old}$ in comparison with

454 observed data at Barrocolorado site in Panama. (a) Simulations LAIs; (b) observation

455 LAIs; and (c) scatterplots between simulated and observed LAIs.

456

457 **4.2 Comparison of patterns of gridded LAI cohort seasonality with climatic and**

458 **phenological patterns**

459 The *in situ* measurements of LAI$_{young}$, LAI$_{mature}$, and LAI$_{old}$ suggested diverse

460 patterns of Lad-LAI seasonality over the TEFs. Nevertheless, the sparse coverage of

461 these sites raised challenging for a comprehensive and direct evaluation of leaf age-

462 dependent LAI seasonality product. To evaluate the robustness of the gridded Lad-LAI

463 seasonality product at the regional scale, we further conducted spatial clustering

464 analyses of LAI$_{young}$, LAI$_{mature}$, and LAI$_{old}$ using the *K*-means analysis method.

465 Surprisingly, the spatial patterns of Lad-LAI product clustered from satellite-based

466 vegetative signals (**Fig. 7 g-i**) coincide well with those clustered from in-dependent

467 climatic variables (rainfall and radiation etc.) (**Fig. 7 a-c**). These patterns are also

468 similar as those of the climate-phenology rhythms mapped by Yang et al. (2021), which

469 suggested different correlations of litterfall seasonality with canopy phenology between

different climate-phenology rhythms (**Fig. 7 d-f**). In central (sub-region S2) and south (sub-region S3) Amazon (**Fig. 7 g**), the seasonality of LAI_{young}, LAI_{mature}, and LAI_{old} (**Fig. 8 b, c**) are similar as those of BR-Sa1 and BR-Sa3 sites. And in subtropical Asia (sub-region S6) (**Fig. 7 i**), the seasonality of three LAI cohorts (**Fig. 8 f**) are similar as those of Din, Gutian and Banna sites. Notably, in the sub-region S8, located geographically between sub-regions S6 and S7, LAI_{young} shows a peak at July and LAI_{mature} shows a bimodal phenology (**Fig. 8 h**). The remaining 4 sub-regions (sub-regions S1, S4, S5, S7) are all located nearby the Equator. The magnitudes of seasonal changes in LAI cohorts are smaller than those in sub-regions S2, S3, S6 and S8 away from the Equator. It is worth noting that for these sub-regions around the Equator there is a bimodal seasonality pattern for LAI_{mature}, with the first peak around March and the second peak around August (**Fig. 8 a, d, e, g**). This is consistent with the findings of Li et al. (2021) which found that tropical and subtropical TEFs changed from a unimodal phenology at higher-latitudes to a bimodal phenology at lower-latitudes.
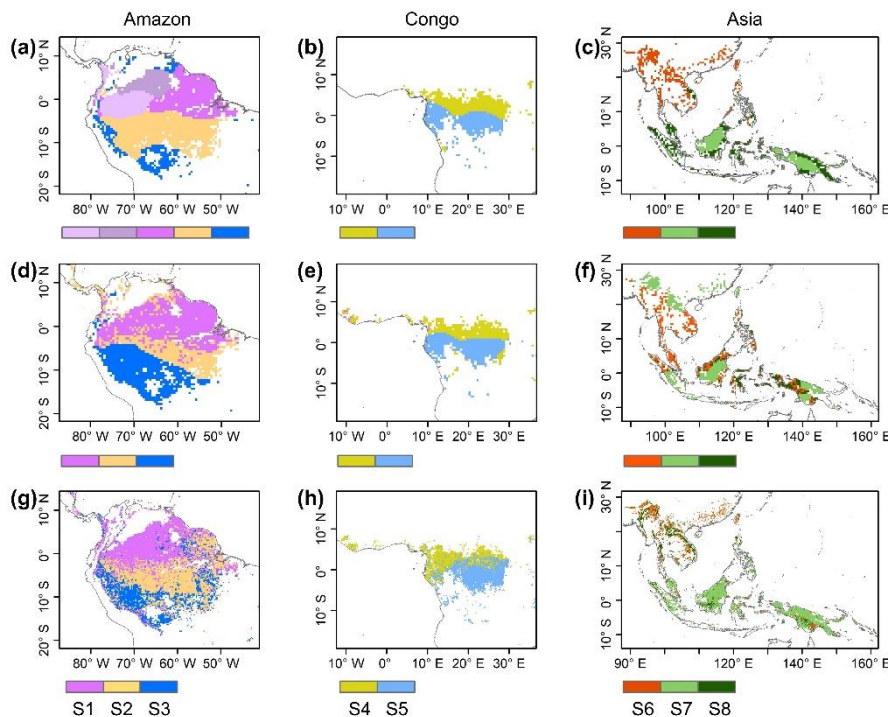
Figure 7. Comparison of sub-regions of Lad-LAI products (plots g-i) with those of climatic factors classified by the K-means clustering analysis (plots a-c) (Chen et al., 2021) and those of the three climate-phenology regimes (plots d-f) developed by Yang

488 et al. (2021).
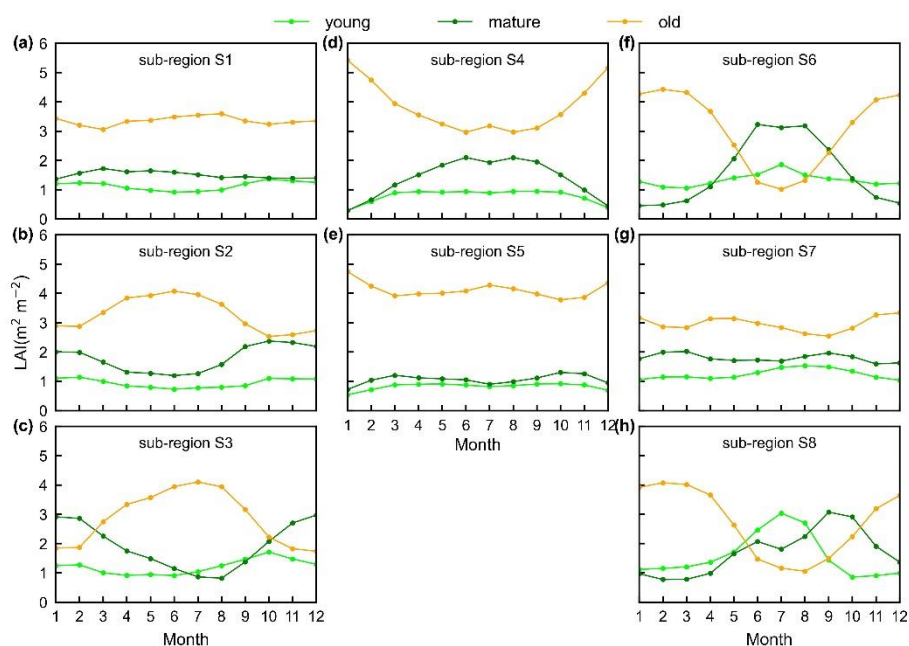
490 **Figure 8.** Seasonality of simulated LAI$_{young}$, LAI$_{mature}$, and LAI$_{old}$ in 8 sub-regions

491 classified by the K-means clustering analysis.

492

493 **4.3 Sub-regional evaluations of gridded LAI$_{young+mature}$ seasonality using satellite-**

494 **based EVI products**

495   The gridded dataset of monthly LAI$_{young+mature}$ was indirectly evaluated using the

496 satellite-based EVI products (Wang et al., 2017; de Moura et al., 2017; Xiao et al., 2005;

497 Wu et al., 2018), as EVI was consistent with LAI$_{young+mature}$ in seasonality (**Figs. S7-S8**),

498 which agreed with previous findings that EVI can be considered as a proxy for leaf area

499 change of those leaves with high photosynthesis efficiency (Huete et al., 2006; Lopes

500 et al., 2016; Wu et al., 2018). It is because that EVI are very sensitive to changes in

501 near-infrared (NIR) reflectance (Galvão et al., 2011) while young and mature leaves

502 also reflect more NIR signals than the older leaves they replace (Toomey et al., 2009).

503 The linear correlation and MSD decompositions (see **Methods**) between simulated and

504 satellite-based EVI were displayed in **Fig. 9**. Overall, the seasonal LAI$_{young+mature}$ is well

505 correlated with satellite-based EVI (R > 0.40) in 78.26% of the TEFs and the average

506 correlation coefficient is equaling to 0.61(**Fig. 9 a-c**). The MSD is smaller than 0.1 in

89.69% of the whole tropical and subtropical TEFs (**Fig. 9 d-f**). Statistics in the 8 clustered sub-regions show that the seasonal $LAI_{young+mature}$ of Lad-LAI data mostly correlate better with seasonal EVI in high-latitude areas (sub-region S2: R=0.65, sub-region S3: R=0.71, sub-region S6: R=0.67) than those in low latitudes (sub-region S1: R=0.46, sub-region S5: R=0.61, sub-region S7: R=0.44, sub-region S8: R=0.64) except for sub-region S4 (R=0.72) (**Figs. 10**, **S9**). The MSD components also confirm a better performance of $LAI_{young+mature}$ seasonality in high-latitude areas (sub-region S2:d_{bias}=0.009, d_{var}=0.001, d_{phase}=0.030; sub-region S3: d_{bias}=0.009, d_{var}=0.002, d_{phase}=0.030; sub-region S6: d_{bias}=0.016, d_{var}=0.005, d_{phase}=0.040) than in low-latitude areas near the Equator (sub-region S1: d_{bias}=0.012, d_{var}=0.001, d_{phase}=0.041; sub-region S4: d_{bias}=0.020, d_{var}=0.001, d_{phase}=0.031; sub-region S5: d_{bias}=0.017, d_{var}=0.001, d_{phase}=0.032; sub-region S7: d_{bias}=0.018, d_{var}=0.002, d_{phase}=0.043; sub-region S8: d_{bias}=0.012, d_{var}=0.005, d_{phase}=0.035) (**Figs. 11**, **S9**). This happens because that the accuracy of Lad-LAI in representing the seasonality of LAI cohorts depends highly on that of input SIF data, which is low sensitive to canopy phenology and shows marginally small seasonal changes nearby the Equator, for example in tropical Asia (Guan et al., 2015; 2016).
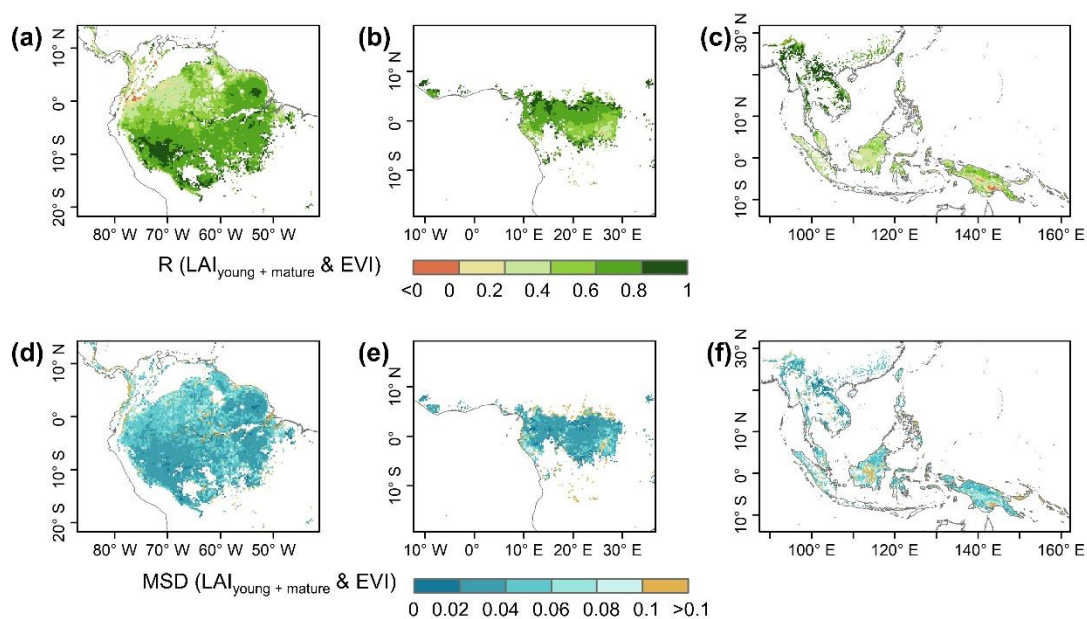
Figure 9. Pearson correlation coefficient (R) and mean squared deviation (MSD)

between seasonality of simulated LAI$_{young+mature}$ and MODIS Enhanced Vegetation Index (EVI).
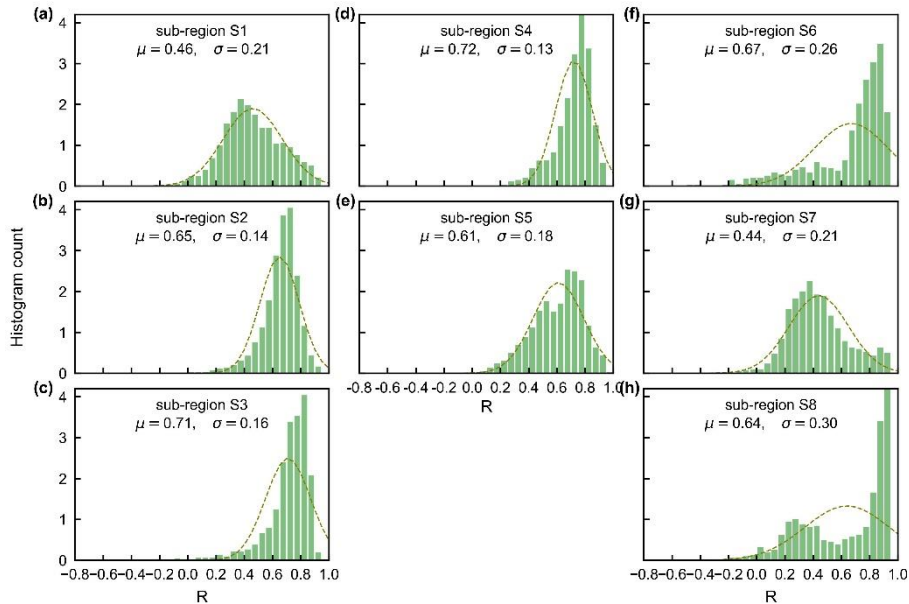
Figure 10. Statistics of the Pearson correlation coefficient (R) between seasonality of simulated LAI$_{young+mature}$ and MODIS Enhanced Vegetation Index (EVI) in the 8 clustered sub-regions.
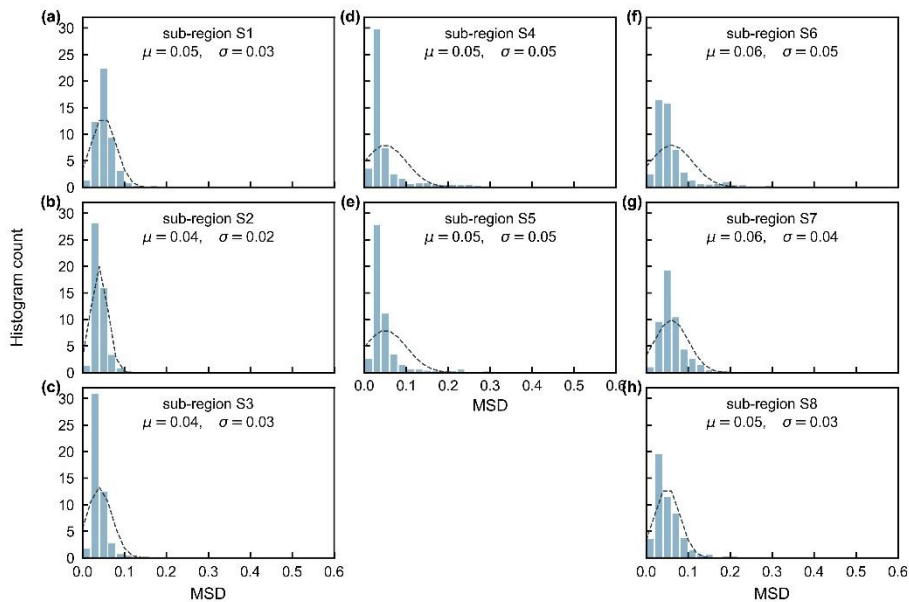
Figure 11. Statistics of the mean squared deviation (MSD) between seasonality of simulated LAI$_{young+mature}$ and MODIS Enhanced Vegetation Index (EVI) in the 8 clustered sub-regions.

538   Additionally, previous studies indicated large-scale green-up area over tropical and

539   subtropical region during the dry seasons (i.e., Guan et al., 2015, Tang et al., 2017,

540   Myneni et al., 2007) where the average annual precipitation exceeds 2,000 mm yr^{-1}.

541   Here, we calculated the differences (Δ) between wet- and dry-season $LAI_{young+mature}$ (i.e.,

542   LAI_{young}+ LAI_{mature}), to test whether the Lad-LAI can capture this green-up spatial

543   pattern. Spatial patterns of $\Delta LAI_{young+mature}$ (**Fig. 12**) are similar to those developed by

544   (Guan et al., 2015), with higher $LAI_{young+mature}$ during the dry season (blue area) in large

545   areas north of the Equator. This indicates an emergence of new leaf flush and increase

546   of mature leaves, resulting the canopy "green-up" phenomenon observed by previous

547   satellite-based signals. It is interesting to note that the total areas (blue regions in **Fig.**

548   **12**) of this dry-season green up shown by $LAI_{young+mature}$ is smaller than those shown by

549   SIF signals that almost everywhere north of the Equator. That is because that new and

550   mature leaves often have a higher photosynthetic capacity than old leaves. A slight or

551   moderate "green-up" in new and mature leaves (i.e., increase in $LAI_{young+mature}$) would

552   boost strong increase in photosynthesis, inducing significant "green-up" shown by

553   photosynthesis-related signals, e.g., SIF data. Therefore, photosynthesis proxies likely

554   overestimate the areas with "green-up" of new leaves during the dry seasons in the real

555   world.
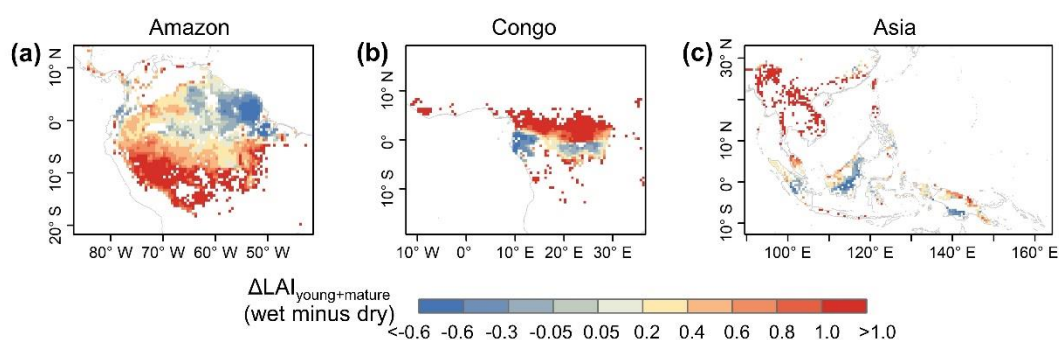
557   **Figure 12**. Spatial pattern of dry-season green-up using wet-season $LAI_{young+mature}$

558   minus dry-season $LAI_{young+mature}$.

559

560   **4.4 Sub-regional evaluations of gridded LAI_{old} seasonality using site-based**

561   **litterfall observations**

562   The seasonal patterns of LAI_{old} were evaluated indirectly using ground-based

563   seasonal litterfall observations from 53 sites over the tropical and subtropical EBFs

564   (black circles in **Fig. 1**, **Figs. S10-S12**), Here, we selected 9 specific sites (**Fig. 13**) with

565   different patterns of litterfall seasonality and LAI_{old} seasonality, to illustrate the

566   analyses results. **Fig. 13 a-i** illustrate the days when there is an abrupt decrease in

567   monthly LAI_{old}, which are closely to monthly litterfall peak. The days when LAI_{old}

568   decreases sharpest (Day_{LAIold}) agree well with the days when their monthly litterfall

569   peaks ($Day_{litterfall}$) (**Fig. 13 j**), mostly distributed near the diagonal lines (R=0.82). This

570   validation from seasonal litterfall data indirectly demonstrate the robustness of the

571   LAI_{old} seasonality of the Lad-LAI product.
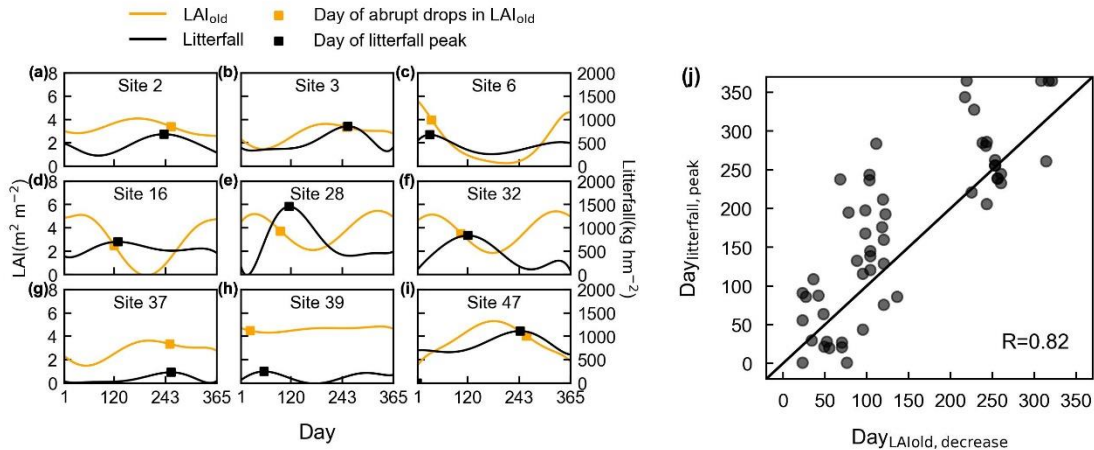
572

573   **Figure 13.** Evaluation of simulated LAI_{old} using ground-observed litterfall seasonality.

574   (a-i) Days of an abrupt decrease in LAI_{old} in comparison with days of corresponding

575   litterfall peak at 9 specific sites for examples. The orange curves represent simulated

576   LAI_{old}. Dots on the orange curves represent the point with an abrupt decrease in LAI_{old}.

577   The black curves represent observed seasonal litterfall mass. The dots on the black

578   curves represent the point with litterfall peak. (j) Comparisons of the days when LAI_{old}

579   has an abrupt decrease (Day_{LAIold}) against the days when monthly litterfall peaks

580   ($Day_{litterfall}$).

581

582   **4.5 Testing potential uncertainties of the Lad-LAI products**

583   To prove the robustness of the neighbor-based decomposition approach, we

584   compared the Lad-LAI products generated based on 2*2 neighboring pixels with those

585   4*4 based on neighboring pixels. Results show that the seasonality of LAI_{young},

586   LAI_{mature} and LAI_{old} in the 0.5-degree Lad-LAI products based on 4*4 neighboring

587   pixels are highly consistent with those of the 0.25-degree one based on 2*2 neighboring

588   pixels across the whole tropical region (**Fig. 14**), with the correlation coefficients (R)

589   being equaling to 0.63, 0.68 and 0.95, respectively (**Fig. S13**).
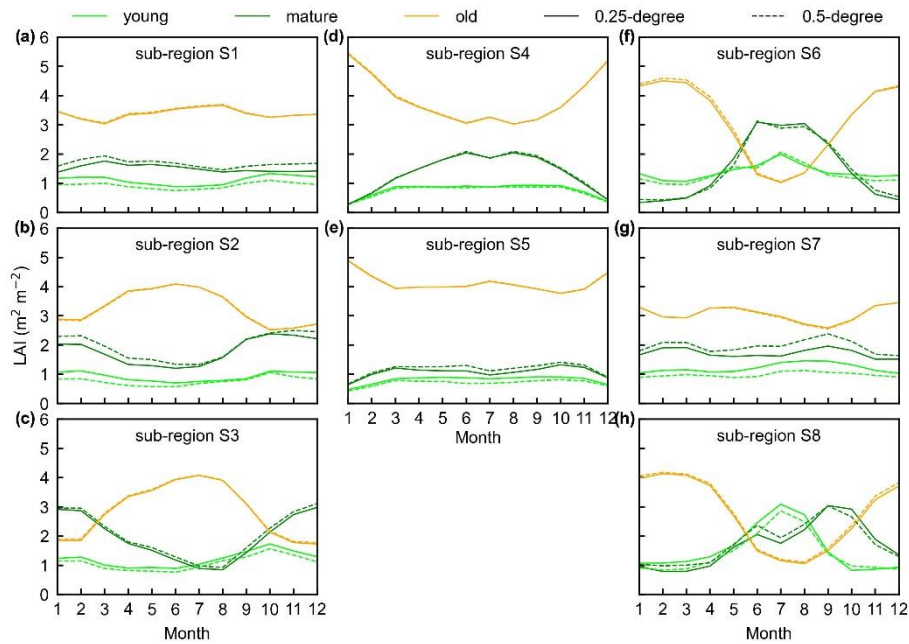
590

591   **Figure 14.** The seasonality of LAI_{young}, LAI_{mature}, LAI_{old} between 0.25-degree and 0.5-

592   degree Lad-LAI datasets in the 8 clustered regions. Limegreen color represents LAI_{young};

593   green color represents LAI_{mature}; and orange color represents LAI_{old}. Solid lines

594   represent 0.25-degree dataset and the dashed lines represent 0.5-degree dataset.

595

596   To test the uncertainties caused by the GPP estimation, we added two more GPP

597   products, i.e., GOSIF-derived GPP (Li and Xiao, 2019) and FLUXCOM GPP (Jung et

598   al., 2019), to produce another two versions of Lad-LAI products. The GPP seasonality

599   coincide well between these three data sources across all the 8 sub-regions (**Fig. S14**).

600   By comparing with the ground-based LAI cohorts at eight observation sites, results

601   show that the Lad-LAI generated from RTSIF-derived GPP show highest correlation

602   and minimal deviation with the *in situ* measurements, with R equaling to 0.36, 0.77 and

603 0.59 and MSD equaling to 0.45, 0.69 and 0.62 for LAI_{young}, LAI_{mature}, and LAI_{old},

604 respectively (**Figs. 15-16**, **S15-S17**). Additionally, we also compared the seasonal

605 variability of LAI_{young}, LAI_{mature}, and LAI_{old} between three Lad-LAI versions in 8 sub-

606 regions classified by the K-means clustering analysis (**Fig. 17**). In general, three

607 versions of Lad-LAI products all performed well in 8 sub-regions with the consistent

608 seasonal variability (**Fig. 17**). On regional average, sub-regions S4, S5, S6, S7 and S8

609 show high consistent seasonality of LAI_{young}, LAI_{mature}, and LAI_{old} between these three

610 products; whereas the Lad-LAI generated from GOSIF-derived GPP performs a little

611 poor in capturing the seasonality of LAI cohorts in Amazon (sub-regions S1, S2 and

612 S3).
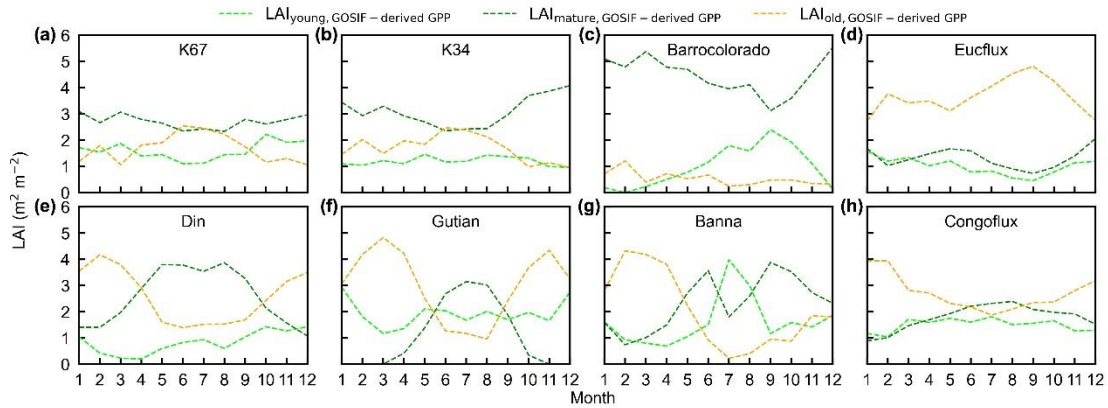
613

614 **Figure 15.** Seasonality of simulated LAI_{young}, LAI_{mature}, and LAI_{old} from GOSIF-

615 derived GPP in comparison with observed data at 8 sites. (a) K67; (b) K34; (c)

616 Barrocolorado; (d) Eucflux; (e) Din; (f) Gutian; (g) Banna; (h) Congoflux.
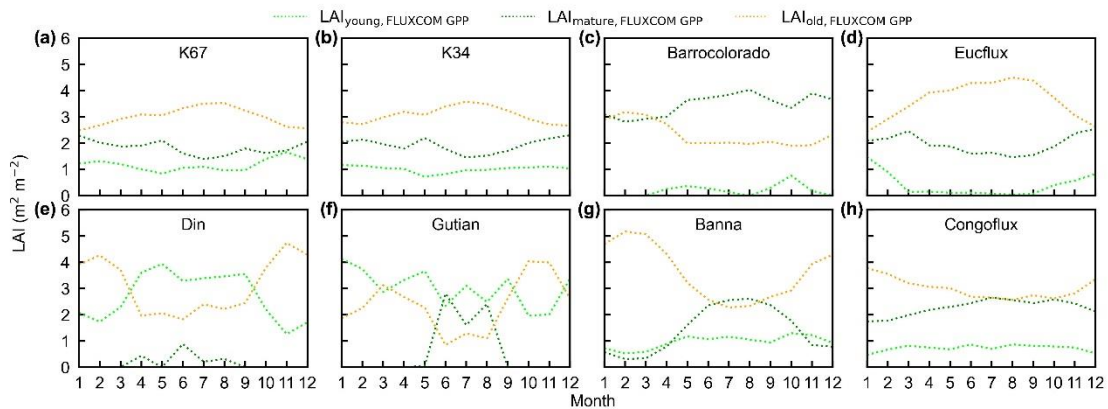
617

618 **Figure 16.** Seasonality of simulated LAI_{young}, LAI_{mature}, and LAI_{old} from FLUXCOM

619 GPP in comparison with observed data at 8 sites. (a) K67; (b) K34; (c) Barrocolorado;

 (d) Eucflux; (e) Din; (f) Gutian; (g) Banna; (h) Congoflux.
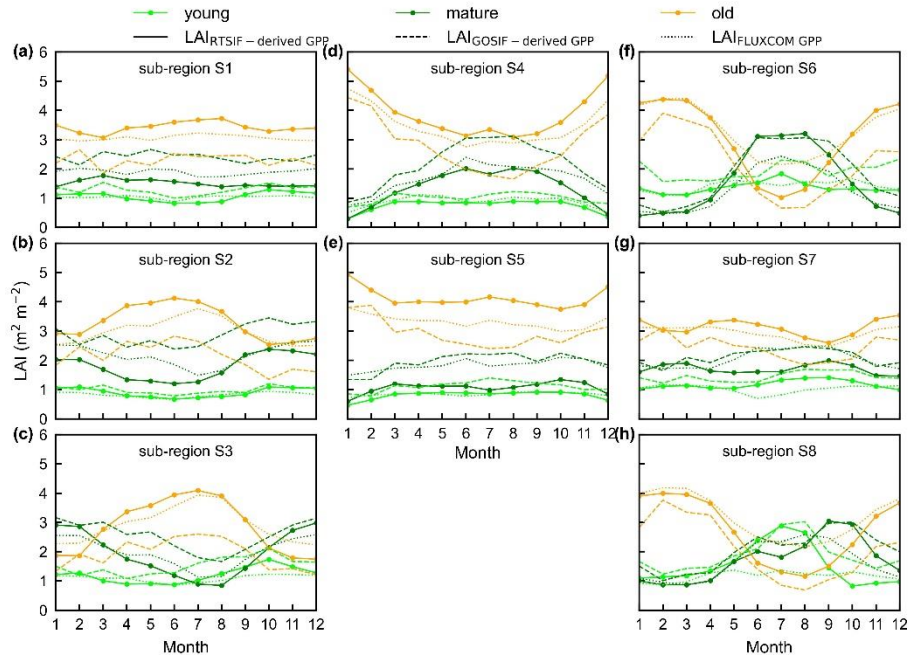
Figure 17. Seasonality of simulated LAI$_{young}$, LAI$_{mature}$, and LAI$_{old}$ from three version products in 8 sub-regions classified by the K-means clustering analysis. Solid lines represent LAI generated from RTSIF-derived GPP; dashed lines represent LAI generated from GOSIF-derived GPP; and dotted lines represent LAI generated from FLUXCOM GPP. Limegreen represents LAI$_{young}$; green represents LAI$_{mature}$; and orange represents LAI$_{old}$.

5 Discussion

Leaf age-dependent LAI performs well in describing the seasonal replacements of canopy leaves in TEFs (Wu et al., 2016; Chen et al., 2020), showing to be a critical plant trait for representing the tropical and subtropical phenology (Doughty and Goulden, 2008; Saleska et al., 2007). However, to our knowledge, there are currently no continental-scale information of such leaf age-dependent LAI data over the whole TEFs, as it can neither be mapped from sparse site observations (Wu et al., 2016), nor can be modeled from ESMs which are triggered by unclear climatic drivers (Chen et al., 2020). These hinder global researches from accurately simulating large-scale photosynthesis (GPP) seasonality using remote sensing approaches and ESMs (Chen et

al., 2020).

The Lad-LAI product developed in this study is the first continental-scale gridded dataset of monthly LAI in different leaf age cohorts. Although still needing more *in situ* observations for an adequate validation, the seasonality of three LAI cohorts performs well at the eight sites (four in south America, three in subtropical Asia and one in Congo) with very fine-scale collections of monthly LAI_{young}, LAI_{mature}, and LAI_{old}. To test the robustness of the gridded Lad-LAI products over the whole TEFs, the seasonality of LAI_{mature} was also validated pixel by pixel using satellite-based EVI products, and the phase of LAI_{old} seasonality were compared with those of seasonal litterfall data from 53 site measurements, respectively. Moreover, the $LAI_{young+mature}$ from the new Lad-LAI products can also directly represent the large-scale dry-season green-up of canopy leaves north of the Equator. Overall, direct and indirect evaluations both demonstrated the robustness of the developed Lad-LAI products.

It should be noted that over the regions with a large magnitude of annual precipitation nearby the Equator, there are no obvious dry seasons, and thus tree canopy phenology changes are smaller than higher-latitude ones throughout the year (Yang et al., 2021). The LAI of young, mature and old leaf cohorts all show a bimodal phenology with marginally small seasonal changes nearby the Equator, which is captured by the developed Lad-LAI product. Secondly, we used a constant coefficient to transfer from SIF data to GPP and also assumed a constant value for the total LAI over the whole TEFs, which might bring additional uncertainties. This can be seen from the MSD evaluations, where the bias-related term dominates the total MSD, especially in regions nearby the Equator. However, this bring less impacts on the seasonality of Lad-LAI, as the phase-related term of MSD is much smaller.

Additionally, the maximum carboxylation rate ($V_{c,max}$) of leaves changes significantly with leaf age (Xu et al., 2017). Currently, most Earth system models (ESMs) define $V_{c,max}$ as a function of leaf age whereas their relationship is still less well understood in TEFs due to sparse in-situ measurements (Chen et al., 2020). This

667 consequentially leads to the poor representation of LAI and GPP seasonality in ESMs

668 (De Weirdt et al., 2012). To overcome this challenge, here we simplified the tree canopy

669 into three big leaves (i.e., young, mature and old) in TEFs, similar as the two-big leaves

670 model developed for temperate and boreal forests (Best et al., 2011; Clark et al., 2011;

671 Harper et al., 2016), which simplified tree canopy into sun and shade leaves. However,

672 some uncertain remains on the assumption, as it neglects the spatial and temporal

673 variations of $V_{c,max}$, which also changes with seasonal climate anomaly and also differs

674 between nearby pixels in high heterogeneous forest ecosystems. This assumption may

675 bring uncertainties for simulating seasonal An and therefore influence the seasonality

676 of Lad-LAI.

677 In summary, we developed a new method to produce the first global gridded dataset

678 of leaf age-dependent LAI product across the whole EBFs over the continental scale.

679 Although some uncertainties might remain, the Lad-LAI products could provide

680 seasonal age-dependent LAI data at the pixel-level to develop a common phenology

681 model for the whole tropical and subtropical EBFs in ESMs that are currently run at a

682 coarser resolution. With the development of remote sensing technology, finer temporal

683 and spatial resolutions of SIF products will enable finer temporal and spatial resolutions

684 maps of Lad-LAI products in the future.

685

686 6. Data availability

687 The 0.25-degree leaf age-dependent LAI seasonality (Lad-LAI) data from 2001-

688 2018 are presented in this paper as the main one, and their time-series are as a

689 supplementary dataset. The two datasets are available at

690 https://doi.org/10.6084/m9.figshare.21700955.v4 (Yang et al., 2022). Besides, we also

691 provided another two versions of Lad-LAI generated from GOSIF-derived GPP and

692 FLUXCOM GPP, respectively. These datasets are compressed in GeoTiff, with a spatial

693 reference of WGS84. Each file in those dataset is named like "LAI_{leaf age}_{spatial

694 resolution}_{month/year-month}.tif".

695

7. Conclusion

This study for the first-time developed a continental-scale gridded dataset of monthly LAI in three leaf age cohorts from 2001-2018 RTSIF data. The LAI seasonality of young, mature and old leaves was evaluated using *in situ* measurements of seasonal LAI data, satellite based EVI and *in situ* measurements of seasonal litterfall data. The evaluations from these datasets demonstrate the robustness of the seasonality of three leaf age cohorts. The new Lad-LAI products indicate diverse patterns over the whole tropical and subtropical regions. In central and south Amazon, LAI_{young} and LAI_{mature} decrease at early dry season around February and start to increase at early wet season around June. On the contrary, in subtropical Asia, LAI_{young} and LAI_{mature} increase during the wet season and peak with largest rainfall at June or July. In regions nearby the Equator, the LAI cohorts show a bimodal phenology but with marginally small changes in the magnitude. The proposed method will enable to produce finer temporal and spatial resolutions maps of Lad-LAI products by using precise temporal and spatial resolutions data as the inputs. The Lad-LAI products will be helpful for diagnosing the adaption of tropical and subtropical forest to climate change; and will also help improve the development of phenology models in ESMs.

Supplement. The supplement related to this article will be available online at once accepted.

Author contributions. XC designed the research and wrote the paper. XY performed the analyses. All the authors edited and revised the paper.

Competing interests. The authors declare no competing interests.

Financial support.

723 This study was supported by the National Natural Science Foundation of China

724 (grant numbers U21A6001, 31971458, 41971275), the Guangdong Major Project of

725 Basic and Applied Basic Research (grant number 2020B0301030004), the Special high-

726 level plan project of Guangdong Province (grant number 2016TQ03Z354), Innovation

727 Group Project of Southern Marine Science and Engineering Guangdong Laboratory

728 (Zhuhai) (grant number 311021009).

729

730 **Acknowledgement**

731 Thanks for Dr. Jin Wu from Hongkong University for providing the observation

732 data of LAI cohorts at K67 and K34 sites in Amazon. We would also like to thank the

733 editor and reviewers for their valuable time in reviewing the manuscript.

734

735 **Reference:**

736 Albert, L. P., Wu, J., Prohaska, N., de Camargo, P. B., Huxman, T. E., Tribuzy, E. S.,
737   Ivanov, V. Y., Oliveira, R. S., Garcia, S., Smith, M. N., Oliveira Junior, R. C.,
738   Restrepo-Coupe, N., da Silva, R., Stark, S. C., Martins, G. A., Penha, D. V., and
739   Saleska, S. R.: Age-dependent leaf physiology and consequences for crown-scale
740   carbon uptake during the dry season in an Amazon evergreen forest, New Phytol,
741   219, 870-884, 10.1111/nph.15056, 2018.
742 Aragao, L. E., Poulter, B., Barlow, J. B., Anderson, L. O., Malhi, Y., Saatchi, S., Phillips,
743   O. L., and Gloor, E.: Environmental change and the carbon balance of Amazonian
744   forests, Biol Rev Camb Philos Soc, 89, 913-931, 10.1111/brv.12088, 2014.
745 Arora, V. K. and Boer, G. J.: Fire as an interactive component of dynamic vegetation
746   models, Journal of Geophysical Research: Biogeosciences, 110, n/a-n/a,
747   10.1029/2005jg000042, 2005.
748 Barlow, J., Gardner, T. A., Ferreira, L. V., and Peres, C. A.: Litter fall and decomposition
749   in primary, secondary and plantation forests in the Brazilian Amazon, Forest
750   Ecology and Management, 247, 91-97, 10.1016/j.foreco.2007.04.017, 2007.
751 Beer, C., Reichstein, M., Tomelleri, E., Ciais, P., Jung, M., Carvalhais, N., Rodenbeck,
752   C., Arain, M. A., Baldocchi, D., Bonan, G. B., Bondeau, A., Cescatti, A., Lasslop,
753   G., Lindroth, A., Lomas, M., Luyssaert, S., Margolis, H., Oleson, K. W., Roupsard,
754   O., Veenendaal, E., Viovy, N., Williams, C., Woodward, F. I., and Papale, D.:
755   Terrestrial gross carbon dioxide uptake: global distribution and covariation with
756   climate, Science, 329, 834-838, 10.1126/science.1184984, 2010.
757 Bernacchi, C. J., Pimentel, C., and Long, S. P.: In vivo temperature response functions
758   of parameters required to model RuBP-limited photosynthesis, Plant, Cell &

Environment, 26, 1419-1430, 10.1046/j.0016-8025.2003.01050.x, 2003.

Bernacchi, C. J., Bagley, J. E., Serbin, S. P., Ruiz-Vera, U. M., Rosenthal, D. M., and Vanloocke, A.: Modelling C(3) photosynthesis from the chloroplast to the ecosystem, Plant Cell Environ, 36, 1641-1657, 10.1111/pce.12118, 2013.

Best, M. J., Pryor, M., Clark, D. B., Rooney, G. G., Essery, R. L. H., Ménard, C. B., Edwards, J. M., Hendry, M. A., Porson, A., Gedney, N., Mercado, L. M., Sitch, S., Blyth, E., Boucher, O., Cox, P. M., Grimmond, C. S. B., and Harding, R. J.: The Joint UK Land Environment Simulator (JULES), model description–Part 1: Energy and water fluxes. Geoscientific Model Development, 4, 677–699, 2011.

Brando, P. M., Goetz, S. J., Baccini, A., Nepstad, D. C., Beck, P. S., and Christman, M. C.: Seasonal and interannual variability of climate and vegetation indices across the Amazon. Proceedings of the National Academy of Sciences, 200908741. 2010.

Chen, X., Huang, Y., Nie, C., Zhang, S., Wang, G., Chen, S., and Chen, Z.: A long-term reconstructed TROPOMI solar-induced fluorescence dataset using machine learning algorithms, Sci Data, 9, 427, 10.1038/s41597-022-01520-1, 2022.

Chen, X., Maignan, F., Viovy, N., Bastos, A., Goll, D., Wu, J., Liu, L., Yue, C., Peng, S., Yuan, W., Conceição, A. C., O'Sullivan, M., and Ciais, P.: Novel Representation of Leaf Phenology Improves Simulation of Amazonian Evergreen Forest Photosynthesis in a Land Surface Model, Journal of Advances in Modeling Earth Systems, 12, 10.1029/2018ms001565, 2020.

Chen, X., Ciais, P., Maignan, F., Zhang, Y., Bastos, A., Liu, L., Bacour, C., Fan, L., Gentine, P., Goll, D., Green, J., Kim, H., Li, L., Liu, Y., Peng, S., Tang, H., Viovy, N., Wigneron, J. P., Wu, J., Yuan, W., and Zhang, H.: Vapor Pressure Deficit and Sunlight Explain Seasonality of Leaf Phenology and Photosynthesis Across Amazonian Evergreen Broadleaved Forest, Global Biogeochemical Cycles, 35, 10.1029/2020gb006893, 2021.

Clark, D. B., Mercado, L. M., Sitch, S., Jones, C. D., Gedney, N., Best, M. J., Pryor, M., Rooney, G. G., Essery, R. L. H., Blyth, E., Boucher, O., Harding, R. J., Huntingford, C., and Cox, P. M.: The Joint UK Land Environment Simulator (JULES), model description–Part 2: Carbon fluxes and vegetation dynamics. Geoscientific Model Development, 4, 701–722, 2011.

Cramer, W., Bondeau, A., Woodward, F. I., Prentice, I. C., Betts, R. A., Brovkin, V., Cox, P. M., Fisher, V., Foley, J. A., Friend, A. D., Kucharik, C., Lomas, M. R., Ramankutty, N., Sitch, S., Smith, B., White, A., and Young-Molling, C.: Global response of terrestrial ecosystem structure and function to CO2 and climate change: results from six dynamic global vegetation models, Global Change Biology, 7, 357-373, 10.1046/j.1365-2486.2001.00383.x, 2001.

Dantas, M. and Phillipson, J.: Litterfall and litter nutrient content in primary and

secondary Amazonian 'terra firme' rain forest, Journal of Tropical Ecology, 5, 27-36, 10.1017/s0266467400003199, 1989.

Davidson, E. A., de Araújo, A. C., Balch, J. K., Brown, I. F., Bustamante, M. M., et al.: The Amazon basin in transition. Nature, 481(7381), 321–328. https://doi.org/10.1038/nature10717. 2012.

de Moura, Y. M., Galvão, L. S., Hilker, T., Wu, J., Saleska, S., do Amaral, C. H., Nelson, B. W., Lopes, A. P., Wiedeman, K. K., Prohaska, N., de Oliveira, R. C., Machado, C. B., and Aragão, L. E. O. C.: Spectral analysis of amazon canopy phenology during the dry season using a tower hyperspectral camera and modis observations, ISPRS Journal of Photogrammetry and Remote Sensing, 131, 52-64, 10.1016/j.isprsjprs.2017.07.006, 2017.

De Weirdt, M., Verbeeck, H., Maignan, F., Peylin, P., Poulter, B., Bonal, D., Ciais, P., and Steppe, K.: Seasonal leaf dynamics for tropical evergreen forests in a process-based global ecosystem model, Geoscientific Model Development, 5, 1091-1108, 10.5194/gmd-5-1091-2012, 2012.

Dechant, B., Ryu, Y., Badgley, G., Zeng, Y., Berry, J. A., Zhang, Y., Goulas, Y., Li, Z., Zhang, Q., Kang, M., Li, J., and Moya, I.: Canopy structure explains the relationship between photosynthesis and sun-induced chlorophyll fluorescence in crops, Remote Sensing of Environment, 241, 10.1016/j.rse.2020.111733, 2020.

Dee, D. P., Uppala, S. M., Simmons, A. J., Berrisford, P., Poli, P., Kobayashi, S., Andrae, U., Balmaseda, M. A., Balsamo, G., Bauer, P., Bechtold, P., Beljaars, A. C. M., van de Berg, L., Bidlot, J., Bormann, N., Delsol, C., Dragani, R., Fuentes, M., Geer, A. J., Haimberger, L., Healy, S. B., Hersbach, H., Hólm, E. V., Isaksen, L., Kållberg, P., Köhler, M., Matricardi, M., McNally, A. P., Monge-Sanz, B. M., Morcrette, J. J., Park, B. K., Peubey, C., de Rosnay, P., Tavolato, C., Thépaut, J. N., and Vitart, F.: The ERA-Interim reanalysis: configuration and performance of the data assimilation system, Quarterly Journal of the Royal Meteorological Society, 137, 553-597, 10.1002/qj.828, 2011.

Doughty, C. E. and Goulden, M. L.: Seasonal patterns of tropical forest leaf area index and CO_2 exchange, Journal of Geophysical Research: Biogeosciences, 113, n/a-n/a, 10.1029/2007jg000590, 2008.

Farquhar, G. D., von Caemmerer, S., and Berry, J. A.: A biochemical model of photosynthetic CO2 assimilation in leaves of C 3 species, Planta, 149, 78-90, 10.1007/BF00386231, 1980.

Galvão, L. S., dos Santos, J. R., Roberts, D. A., Breunig, F. M., Toomey, M., and de Moura, Y. M.: On intra-annual EVI variability in the dry season of tropical forest: a case study with MODIS and hyperspectral data. Remote Sens. Environ. 115, 2350–2359, 2011.

Guan, K., Berry, J. A., Zhang, Y., Joiner, J., Guanter, L., Badgley, G. and Lobell, D.B.: Improving the monitoring of crop productivity using spaceborne solar-induced fluorescence. Global change biology, 22(2), 716-726. 2016.

Guan, K., Pan, M., Li, H., Wolf, A., Wu, J., Medvigy, D., Caylor, K. K., Sheffield, J.,

Wood, E. F., Malhi, Y., Liang, M., Kimball, J. S., Saleska, Scott R., Berry, J., Joiner, J., and Lyapustin, A. I.: Photosynthetic seasonality of global tropical forests constrained by hydroclimate, Nature Geoscience, 8, 284-289, 10.1038/ngeo2382, 2015.

Harper, A. B., Cox, P. M., Friedlingstein, P., Wiltshire, A. J., Jones, C. D., Sitch, S., Mercado, L. M., Groenendijk, M., Robertson, E., Kattge, J., Bönisch, G., Atkin, O. K., Bahn, M., Cornelissen, J., Niinemets, Ü., Onipchenko, V., Peñuelas, J., Poorter, L., Reich, P. B., Soudzilovskaia, N. A., and Bodegom, P. V.: Improved representation of plant functional types and physiology in the Joint UK Land Environment Simulator (JULES v4.2) using plant trait information. Geoscientific Model Development Discussions, 9, 2415–2440, 2016.

Huete, A., Didan, K., Miura, T., Rodriguez, E. P., Gao, X., and Ferreira, L. G.: Overview of the radiometric and biophysical performance of the MODIS vegetation indices, Remote Sensing of Environment, 83, 195-213, 10.1016/s0034-4257(02)00096-2, 2002.

Huete, A. R., Didan, K., Shimabukuro, Y. E., Ratana, P., Saleska, S. R., Hutyra, L. R., Yang, W., Nemani, R. R., and Myneni, R.: Amazon rainforests green-up with sunlight in dry season, Geophysical Research Letters, 33, 10.1029/2005gl025583, 2006.

June, T., Evans, J. R., and Farquhar, G. D.: A simple new equation for the reversible temperature dependence of photosynthetic electron transport: a study on soybean leaf, Funct Plant Biol, 31, 275-283, 10.1071/FP03250, 2004.

Jung, M., Koirala, S., Weber, U., Ichii, K., Gans, F., Camps-Valls, G., Papale, D., Schwalm, C., Tramontana, G., and Reichstein, M.: The FLUXCOM ensemble of global land-atmosphere energy fluxes. Sci Data 6, 74. https://doi.org/10.1038/s41597-019-0076-8. 2019.

Kartikeyan, B., Sarkar, A., and Majumder, K. L.: A segmentation approach to classification of remote sensing imagery, International Journal of Remote Sensing, 19, 1695-1709, 1998.

Kobayashi, K. and Salam, M. U.: Comparing Simulated and Measured Values Using Mean Squared Deviation and its Components, Agronomy Journal, 92, 10.1007/s100870050043, 2000.

Leff, J. W., Wieder, W. R., Taylor, P. G., Townsend, A. R., Nemergut, D. R., Grandy, A. S., and Cleveland, C. C.: Experimental litterfall manipulation drives large and rapid changes in soil carbon cycling in a wet tropical forest. Global Change Biology, 18(9), 2969–2979. https://doi.org/10.1111/j.1365-2486.2012.02749.x. 2012.

Li, Q., Chen, X., Yuan, W., Lu, H., Shen, R., Wu, S., Gong, F., Dai, Y., Liu, L., Sun, Q., Zhang, C., and Su, Y.: Remote Sensing of Seasonal Climatic Constraints on Leaf Phenology Across Pantropical Evergreen Forest Biome, Earth's Future, 9, 10.1029/2021ef002160, 2021.

Li, X., and Xiao, J.: Mapping photosynthesis solely from solar-induced chlorophyll

881   fluorescence: A global, fine-resolution dataset of gross primary production derived
882   from OCO-2. Remote Sensing, 11(21), 2563; https://doi.org/10.3390/rs11212563.
883   2019.
884 Lin, Y.-S., Medlyn, B. E., Duursma, R. A., Prentice, I. C., Wang, H., Baig, S., Eamus,
885   D., de Dios, Victor R., Mitchell, P., Ellsworth, D. S., de Beeck, M. O., Wallin, G.,
886   Uddling, J., Tarvainen, L., Linderson, M.-L., Cernusak, L. A., Nippert, J. B.,
887   Ocheltree, T. W., Tissue, D. T., Martin-StPaul, N. K., Rogers, A., Warren, J. M.,
888   De Angelis, P., Hikosaka, K., Han, Q., Onoda, Y., Gimeno, T. E., Barton, C. V. M.,
889   Bennie, J., Bonal, D., Bosc, A., Löw, M., Macinins-Ng, C., Rey, A., Rowland, L.,
890   Setterfield, S. A., Tausz-Posch, S., Zaragoza-Castells, J., Broadmeadow, M. S. J.,
891   Drake, J. E., Freeman, M., Ghannoum, O., Hutley, Lindsay B., Kelly, J. W.,
892   Kikuzawa, K., Kolari, P., Koyama, K., Limousin, J.-M., Meir, P., Lola da Costa,
893   A. C., Mikkelsen, T. N., Salinas, N., Sun, W., and Wingate, L.: Optimal stomatal
894   behaviour around the world, Nature Climate Change, 5, 459-464,
895   10.1038/nclimate2550, 2015.
896 Lopes, A. P., Nelson, B. W., Wu, J., Graça, P. M. L. d. A., Tavares, J. V., Prohaska, N.,
897   Martins, G. A., and Saleska, S. R.: Leaf flush drives dry season green-up of the
898   Central Amazon, Remote Sensing of Environment, 182, 90-98,
899   10.1016/j.rse.2016.05.009, 2016.
900 Maes, W. H., Gentine, P., Verhoest, N. E. C., and Miralles, D. G.: Potential evaporation
901   at eddy-covariance sites across the globe, Hydrology and Earth System Sciences,
902   23, 925-948, 10.5194/hess-23-925-2019, 2019.
903 Medlyn, B. E., Duursma, R. A., Eamus, D., Ellsworth, D. S., Prentice, I. C., Barton, C.
904   V. M., Crous, K. Y., De Angelis, P., Freeman, M., and Wingate, L.: Reconciling
905   the optimal and empirical approaches to modelling stomatal conductance, Global
906   Change Biology, 17, 2134-2144, 10.1111/j.1365-2486.2010.02375.x, 2011.
907 Melgosa, M., Huertas, R., and Berns, R. S.: Performance of recent advanced color-
908   difference formulas using the standardized residual sum of squares index. Journal
909   of the Optical Society of America A, 25(7), 1828-1834.
910   https://doi.org/10.1364/JOSAA.25.001828. 2008
911 Menezes, J., Garcia, S., Grandis, A., Nascimento, H., Domingues, T. F., Guedes, A. V.,
912   Aleixo, I., Camargo, P., Campos, J., Damasceno, A., Dias-Silva, R., Fleischer, K.,
913   Kruijt, B., Cordeiro, A. L., Martins, N. P., Meir, P., Norby, R. J., Pereira, I., Portela,
914   B., Rammig, A., Ribeiro, A. G., Lapola, D. M., and Quesada, C. A.: Changes in
915   leaf functional traits with leaf age: when do leaves decrease their photosynthetic
916   capacity in Amazonian trees? Tree Physiology, 42(5), 922-938,
917   https://doi.org/10.1093/treephys/tpab042, 2021.
918 Merkl, R. and Waack, S.: Bioinformatik interaktiv, John Wiley & Sons, 2009.
919 Midoko Iponga, D., Mpikou, R. G. J., Loumeto, J., and Picard, N.: The effect of
920   different anthropogenic disturbances on litterfall of a dominant pioneer rain forest
921   tree in Gabon, African Journal of Ecology, 58, 281-290, 10.1111/aje.12696, 2019.
922 Myneni, R. B., Yang, W., Nemani, R. R., Huete, A. R., Dickinson, R. E., Knyazikhin,

Y., Didan, K., Fu, R., Negrón Juárez, R. I., Saatchi, S. S., Hashimoto, H., Ichii, K., Shabanov, N. V., Tan, B., Ratana, P., Privette, J. L., Morisette, J. T., Vermote, E. F., Roy, D. P., Wolfe, R. E., Friedl, M. A., Running, S. W., Votava, P., El-Saleous, N., Devadiga, S., Su, Y., and Salomonson, V. V.: Large seasonal swings in leaf area of Amazon rainforests. Proc. Natl Acad. Sci. USA, 104, 4820–4823. 2007.

Ndakara, O. E.: Litterfall and Nutrient Returns in Isolated Stands of Persea gratissima (Avocado Pear) in the Rainforest Zone of Southern Nigeria, Ethiopian Journal of Environmental Studies and Management, 4, 10.4314/ejesm.v4i3.6, 2011.

Pastorello, G., Trotta, C., Canfora, E., Chu, H., Christianson, D., Cheah, Y. W., Poindexter, C., Chen, J., Elbashandy, A., Humphrey, M., Isaac, P., Polidori, D., Reichstein, M., Ribeca, A., van Ingen, C., Vuichard, N., Zhang, L., Amiro, B., Ammann, C., Arain, M. A., Ardo, J., Arkebauer, T., Arndt, S. K., Arriga, N., Aubinet, M., Aurela, M., Baldocchi, D., Barr, A., Beamesderfer, E., Marchesini, L. B., Bergeron, O., Beringer, J., Bernhofer, C., Berveiller, D., Billesbach, D., Black, T. A., Blanken, P. D., Bohrer, G., Boike, J., Bolstad, P. V., Bonal, D., Bonnefond, J. M., Bowling, D. R., Bracho, R., Brodeur, J., Brummer, C., Buchmann, N., Burban, B., Burns, S. P., Buysse, P., Cale, P., Cavagna, M., Cellier, P., Chen, S., Chini, I., Christensen, T. R., Cleverly, J., Collalti, A., Consalvo, C., Cook, B. D., Cook, D., Coursolle, C., Cremonese, E., Curtis, P. S., D'Andrea, E., da Rocha, H., Dai, X., Davis, K. J., Cinti, B., Grandcourt, A., Ligne, A., De Oliveira, R. C., Delpierre, N., Desai, A. R., Di Bella, C. M., Tommasi, P. D., Dolman, H., Domingo, F., Dong, G., Dore, S., Duce, P., Dufrene, E., Dunn, A., Dusek, J., Eamus, D., Eichelmann, U., ElKhidir, H. A. M., Eugster, W., Ewenz, C. M., Ewers, B., Famulari, D., Fares, S., Feigenwinter, I., Feitz, A., Fensholt, R., Filippa, G., Fischer, M., Frank, J., Galvagno, M., Gharun, M., Gianelle, D., Gielen, B., Gioli, B., Gitelson, A., Goded, I., Goeckede, M., Goldstein, A. H., Gough, C. M., Goulden, M. L., Graf, A., Griebel, A., Gruening, C., Grunwald, T., Hammerle, A., Han, S., Han, X., Hansen, B. U., Hanson, C., Hatakka, J., He, Y., Hehn, M., Heinesch, B., Hinko-Najera, N., Hortnagl, L., Hutley, L., Ibrom, A., Ikawa, H., Jackowicz-Korczynski, M., Janous, D., Jans, W., Jassal, R., Jiang, S., Kato, T., Khomik, M., Klatt, J., Knohl, A., Knox, S., Kobayashi, H., Koerber, G., Kolle, O., Kosugi, Y., Kotani, A., Kowalski, A., Kruijt, B., Kurbatova, J., Kutsch, W. L., Kwon, H., Launiainen, S., Laurila, T., Law, B., Leuning, R., Li, Y., Liddell, M., Limousin, J. M., Lion, M., Liska, A. J., Lohila, A., Lopez-Ballesteros, A., Lopez-Blanco, E., Loubet, B., Loustau, D., Lucas-Moffat, A., Luers, J., Ma, S., Macfarlane, C., Magliulo, V., Maier, R., Mammarella, I., Manca, G., Marcolla, B., Margolis, H. A., Marras, S., Massman, W., Mastepanov, M., Matamala, R., Matthes, J. H., Mazzenga, F., McCaughey, H., McHugh, I., McMillan, A. M. S., Merbold, L., Meyer, W., Meyers, T., Miller, S. D., Minerbi, S., Moderow, U., Monson, R. K., Montagnani, L., Moore, C. E., Moors, E., Moreaux, V., Moureaux, C., Munger, J. W., Nakai, T., Neirynck, J., Nesic, Z., Nicolini, G., Noormets, A., Northwood, M., Nosetto, M., Nouvellon, Y., Novick, K., Oechel, W., Olesen, J. E.,

Ourcival, J. M., Papuga, S. A., Parmentier, F. J., Paul-Limoges, E., Pavelka, M., Peichl, M., Pendall, E., Phillips, R. P., Pilegaard, K., Pirk, N., Posse, G., Powell, T., Prasse, H., Prober, S. M., Rambal, S., Rannik, U., Raz-Yaseef, N., Rebmann, C., Reed, D., Dios, V. R., Restrepo-Coupe, N., Reverter, B. R., Roland, M., Sabbatini, S., Sachs, T., Saleska, S. R., Sanchez-Canete, E. P., Sanchez-Mejia, Z. M., Schmid, H. P., Schmidt, M., Schneider, K., Schrader, F., Schroder, I., Scott, R. L., Sedlak, P., Serrano-Ortiz, P., Shao, C., Shi, P., Shironya, I., Siebicke, L., Sigut, L., Silberstein, R., Sirca, C., Spano, D., Steinbrecher, R., Stevens, R. M., Sturtevant, C., Suyker, A., Tagesson, T., Takanashi, S., Tang, Y., Tapper, N., Thom, J., Tomassucci, M., Tuovinen, J. P., Urbanski, S., Valentini, R., van der Molen, M., van Gorsel, E., van Huissteden, K., Varlagin, A., Verfaillie, J., Vesala, T., Vincke, C., Vitale, D., Vygodskaya, N., Walker, J. P., Walter-Shea, E., Wang, H., Weber, R., Westermann, S., Wille, C., Wofsy, S., Wohlfahrt, G., Wolf, S., Woodgate, W., Li, Y., Zampedri, R., Zhang, J., Zhou, G., Zona, D., Agarwal, D., Biraud, S., Torn, M., and Papale, D.: The FLUXNET2015 dataset and the ONEFlux processing pipeline for eddy covariance data, Sci Data, 7, 225, 10.1038/s41597-020-0534-3, 2020.

Pan, Y., Birdsey, R. A., Fang, J., Houghton, R., Kauppi, P. E., Kurz, W. A., et al.: A large and persistent carbon sink in the world's forests. Science, 333(6045), 988–993. https://doi.org/10.1126/science.1201609, 2011.

Pearson, K.: VII. Mathematical contributions to the theory of evolution.—III. Regression, heredity, and panmixia, Philosophical Transactions of the Royal Society of London. Series A, Containing Papers of a Mathematical or Physical Character, 187, 253-318, 10.1098/rsta.1896.0007, 1896.

Piao, S., Fang, J., Zhou, L., Ciais, P. and Zhu, B.: Variations in satellite-derived phenology in China's temperate vegetation. Global Change Biology, 12: 672-685. https://doi.org/10.1111/j.1365-2486.2006.01123.x. 2006.

Restrepo-Coupe, N., Levine, N. M., Christoffersen, B. O., Albert, L. P., Wu, J., Costa, M. H., Galbraith, D., Imbuzeiro, H., Martins, G., da Araujo, A. C., Malhi, Y. S., Zeng, X., Moorcroft, P., and Saleska, S. R.: Do dynamic global vegetation models capture the seasonality of carbon fluxes in the Amazon basin? A data-model intercomparison, Glob Chang Biol, 23, 191-208, 10.1111/gcb.13442, 2017.

Ryu, Y., Baldocchi, D. D., Kobayashi, H., van Ingen, C., Li, J., Black, T. A., Beringer, J., van Gorsel, E., Knohl, A., Law, B. E., and Roupsard, O.: Integration of MODIS land and atmosphere products with a coupled-process model to estimate gross primary productivity and evapotranspiration from 1 km to global scales, Global Biogeochemical Cycles, 25, n/a-n/a, 10.1029/2011gb004053, 2011.

Ryu, Y., Jiang, C., Kobayashi, H., and Detto, M.: MODIS-derived global land products of shortwave radiation and diffuse and total photosynthetically active radiation at 5 km resolution from 2000, Remote Sensing of Environment, 204, 812-825, 10.1016/j.rse.2017.09.021, 2018.

Saatchi, S. S., Harris, N. L., Brown, S., Lefsky, M., Mitchard, E. T., Salas, W., Zutta, B. R., Buermann, W., Lewis, S. L., Hagen, S., Petrova, S., White, L., Silman, M., and

Morel, A.: Benchmark map of forest carbon stocks in tropical regions across three continents, Proc Natl Acad Sci U S A, 108, 9899-9904, 10.1073/pnas.1019576108, 2011.

Saleska, S. R., Didan, K., Huete, A. R., and da Rocha, H. R.: Amazon forests green-up during 2005 drought, Science, 318, 612, 10.1126/science.1146663, 2007.

Saleska, S. R., Wu, J., Guan, K., Araujo, A. C., Huete, A., Nobre, A. D., and Restrepo-Coupe, N.: Dry-season greening of Amazon forests, Nature, 531, E4-5, 10.1038/nature16457, 2016.

Saleska, S. R., Miller, S. D., Matross, D. M., Goulden, M. L., Wofsy, S. C., da Rocha, H. R., de Camargo, P. B., Crill, P., Daube, B. C., de Freitas, H. C., Hutyra, L., Keller, M., Kirchhoff, V., Menton, M., Munger, J. W., Pyle, E. H., Rice, A. H., and Silva, H.: Carbon in Amazon forests: unexpected seasonal fluxes and disturbance-induced losses, Science, 302, 1554-1557, 10.1126/science.1091165, 2003.

Sayer, E. J., Heard, M. S., Grant, H. K., Marthews, T. R., and Tanner, E. V. J.: Soil carbon release enhanced by increased tropical forest litterfall. Nature Climate Change, 1(6), 304–307. https://doi.org/10.1038/nclimate1190. 2011.

Smith, M. N., Stark, S. C., Taylor, T. C., Ferreira, M. L., de Oliveira, E., Restrepo-Coupe, N., Chen, S., Woodcock, T., dos Santos, D. B., Alves, L. F., Figueira, M., de Camargo, P. B., de Oliveira, R. C., Aragão, L. E. O. C., Falk, D. A., McMahon, S. M., Huxman, T. E. and Saleska, S. R.: Seasonal and drought-related changes in leaf area profiles depend on height and light environment in an Amazon forest. New Phytol, 222: 1284-1297. https://doi.org/10.1111/nph.15726. 2019.

Sulla-Menashe, D., Woodcock, C. E., and Friedl, M. A.: Canadian boreal forest greening and browning trends: An analysis of biogeographic patterns and the relative roles of disturbance versus climate drivers. Environmental Research Letters, 13(1), 014007, 2018.

Tang, H., and Dubayah, R.: Light-driven growth in Amazon evergreen forests explained by seasonal variations of vertical canopy structure. Proceedings of the National Academy of Sciences of the United States of America, 114(10), 2640–2644. https://doi.org/10.1073/ pnas.1616943114. 2017.

Toomey, M., Roberts, D. A. and Nelson, B.: The influence of epiphylls on remote sensing of humid forests. Remote Sens. Environ, 113, 1787–1798. 2009.

Wang, C., Li, J., Liu, Q., Zhong, B., Wu, S., and Xia, C.: Analysis of Differences in Phenology Extracted from the Enhanced Vegetation Index and the Leaf Area Index, Sensors (Basel), 17, 10.3390/s17091982, 2017.

Weiss, A. and Norman, J. M.: Partitioning solar radiation into direct and diffuse, visible and near-infrared components, Agricultural and Forest Meteorology, 34, 205-213, 10.1016/0168-1923(85)90020-6, 1985.

Wu, J., Serbin, S. P., Xu, X., Albert, L. P., Chen, M., Meng, R., Saleska, S. R., and Rogers, A.: The phenology of leaf quality and its within-canopy variation is essential for accurate modeling of photosynthesis in tropical evergreen forests, Glob Chang Biol, 23, 4814-4827, 10.1111/gcb.13725, 2017.

Wu, J., Kobayashi, H., Stark, S. C., Meng, R., Guan, K., Tran, N. N., Gao, S., Yang, W., Restrepo-Coupe, N., Miura, T., Oliviera, R. C., Rogers, A., Dye, D. G., Nelson, B. W., Serbin, S. P., Huete, A. R., and Saleska, S. R.: Biological processes dominate seasonality of remotely sensed canopy greenness in an Amazon evergreen forest, New Phytol, 217, 1507-1520, 10.1111/nph.14939, 2018.

Wu, J., Albert, L. P., Lopes, A. P., Restrepo-Coupe, N., Hayek, M., Wiedemann, K. T., Guan, K., Stark, S. C., Christoffersen, B., Prohaska, N., Tavares, J. V., Marostica, S., Kobayashi, H., Ferreira, M. L., Campos, K. S., da Silva, R., Brando, P. M., Dye, D. G., Huxman, T. E., Huete, A. R., Nelson, B. W., and Saleska, S. R.: Leaf development and demography explain photosynthetic seasonality in Amazon evergreen forests, Science, 351, 972-976, 10.1126/science.aad5068, 2016.

Xiao, X., Zhang, Q., Saleska, S., Hutyra, L., De Camargo, P., Wofsy, S., Frolking, S., Boles, S., Keller, M., and Moore, B.: Satellite-based modeling of gross primary production in a seasonally moist tropical evergreen forest, Remote Sensing of Environment, 94, 105-122, 10.1016/j.rse.2004.08.015, 2005.

Xu, L., Saatchi, S. S., Yang, Y., Myneni, R. B., Frankenberg, C., Chowdhury, D., and Bi, J.: Satellite observation of tropical forest seasonality: spatial patterns of carbon exchange in Amazonia, Environmental Research Letters, 10, 10.1088/1748-9326/10/8/084005, 2015.

Xu, X., Medvigy, D., Joseph Wright, S., Kitajima, K., Wu, J., Albert, L. P., Martins, G. A., Saleska, S. R., and Pacala, S. W.: Variations of leaf longevity in tropical moist forests predicted by a trait-driven carbon optimality model, Ecol Lett, 20, 1097-1106, 10.1111/ele.12804, 2017.

Yang, X., Tang, J., Mustard, J. F., Lee, J.-E., Rossini, M., Joiner, J., Munger, J. W., Kornfeld, A., and Richardson, A. D.: Solar-induced chlorophyll fluorescence that correlates with canopy photosynthesis on diurnal and seasonal scales in a temperate deciduous forest, Geophysical Research Letters, 42, 2977-2987, 10.1002/2015gl063201, 2015.

Yang, X., Wu, J., Chen, X., Ciais, P., Maignan, F., Yuan, W., Piao, S., Yang, S., Gong, F., Su, Y., Dai, Y., Liu, L., Zhang, H., Bonal, D., Liu, H., Chen, G., Lu, H., Wu, S., Fan, L., Gentine, P., and Wright, S. J.: A comprehensive framework for seasonal controls of leaf abscission and productivity in evergreen broadleaved tropical and subtropical forests, Innovation (Camb), 2, 100154, 10.1016/j.xinn.2021.100154, 2021.

Yang, X., Chen, X., Ren, J., Yuan, W., Liu, L., Liu, J., Chen, D., Xiao, Y., Wu, S., Fan, L., Dai, X., Su, Y.: Leaf age-dependent LAI seasonality product (Lad-LAI) over tropical and subtropical evergreen broadleaved forests. figshare. Dataset. https://doi.org/10.6084/m9.figshare.21700955.v4. 2022.

Yuan, W., Zheng, Y., Piao, S., Ciais, P., Lombardozzi, D., Wang, Y., Ryu, Y., Chen, G., Dong, W., Hu, Z., Jain, A. K., Jiang, C., Kato, E., Li, S., Lienert, S., Liu, S., Nabel, J., Qin, Z., Quine, T., Sitch, S., Smith, W. K., Wang, F., Wu, C., Xiao, Z., and Yang, S.: Increased atmospheric vapor pressure deficit reduces global vegetation growth,

1091   Sci Adv, 5, eaax1396, 10.1126/sciadv.aax1396, 2019.

1092   Zhao, P., Gao, L., Wei, J., Ma, M., Deng, H., Gao, J., and Chen, X.: Evaluation of ERA-

1093   Interim Air Temperature Data over the Qilian Mountains of China. Advances in

1094   Meteorology, 7353482. https://doi.org/10.1155/2020/7353482, 2020